



## Characterizing the Main Himalayan Thrust in the Garhwal Himalaya, India with receiver function CCP stacking

Warren B. Caldwell<sup>a,\*</sup>, Simon L. Klemperer<sup>a</sup>, Jesse F. Lawrence<sup>a</sup>, Shyam S. Rai<sup>b</sup>, Ashish<sup>c</sup>

<sup>a</sup> Stanford University, Stanford, CA, United States

<sup>b</sup> National Geophysical Research Institute, Hyderabad, India

<sup>c</sup> CSIR Centre for Mathematical Modeling and Computer Simulation, NAL Belur, Bangalore, India

### ARTICLE INFO

#### Article history:

Received 20 November 2012

Received in revised form

10 February 2013

Accepted 11 February 2013

Editor: T.M. Harrison

#### Keywords:

Himalaya

India

Garhwal

receiver functions

CCP stacking

### ABSTRACT

We use common conversion point (CCP) stacking of *P<sub>s</sub>* receiver functions to image the crustal structure and Moho of the Garhwal Himalaya of India. Our seismic array of 21 broadband seismometers spanned the Himalayan thrust wedge at 79–80°E, between the Main Frontal Thrust and the South Tibet Detachment, in 2005–2006. Our CCP image shows the Main Himalayan Thrust (MHT), the detachment at the base of the Himalayan thrust wedge, with a flat-ramp-flat geometry. Seismic impedance contrasts inferred from geologic cross-sections in Garhwal imply a negative impedance contrast (velocity decreasing downward) for the upper flat, located beneath the Lower Himalaya, and a positive impedance contrast (velocity increasing downward) for the ramp, located beneath the surface trace of the Munsiri Thrust (or MCT-I). At the lower flat, located beneath the Higher Himalaya, spatially coincident measurements of very high electrical conductivities require the presence of free fluids, and we infer a negative impedance contrast on the MHT caused by ponding of these fluids beneath the detachment. Our seismic image indicates that the upper flat of the MHT is ~10 km below sea level and dips north at ~2°, connecting to a mid-crustal ramp which is ~10 km high and dips at ~16°. The lower flat is 20–25 km below sea level and dips at ~4°. The Main Central Thrust (MCT) appears as a negative impedance contrast, dipping at ~16°. The Moho is nearly horizontal at 35–45 km depth beneath the Sub-Himalaya and Lower Himalaya, deepening to 50 km or more beneath the Higher Himalaya. This depth is 10–25 km shallower than in the NW Indian Himalaya and 5–10 km shallower than in central Nepal, requiring significant along-strike variations in crustal thickness. The observed thickness of subducted Indian crust in Garhwal is 20–28 km.

© 2013 Elsevier B.V. All rights reserved.

### 1. Introduction

In Earth's greatest active continent–continent collision, subducting Indian crust is bounded above by the Main Himalayan Thrust and below by the Moho. Imaging these boundaries and the geometry of continental subduction has been a long-standing challenge for geophysicists. Some seismic receiver-function studies successfully image the Main Himalayan Thrust (MHT), the detachment at the base of the Himalayan thrust wedge, and place it at between 10 and 15 km depth beneath the Lower Himalaya and at between 15 and 25 km depth beneath the Higher Himalaya, in a smoothly deepening geometry (Nábělek et al., 2009; Schulte-Pelkum et al., 2005; Acton et al., 2010) (Fig. 1a). Its exact depth in these studies depends on which seismic converter is interpreted to represent the MHT. Magnetotelluric profiles

provide complementary information, but the interpreted depth of the MHT on these profiles depends on whether the MHT is inferred to pass above, through, or below the conductivity anomalies (Lemonnier et al., 1999; Israil et al., 2008; Rawat and Arora, in preparation).

A mid-crustal ramp structure in the MHT has been proposed in central Nepal based on the concentration of micro-seismicity (Pandey et al., 1995), uplift of fluvial terraces (Lavé and Avouac, 2001), geodetically determined uplift rates (Berger et al., 2004), and elevated electrical conductivity (Lemonnier et al., 1999). This inferred mid-crustal ramp, although varying somewhat along strike in its location and dip (Berger et al., 2004; Robert et al., 2011), is located approximately beneath the physiographic boundary between the Lower and Higher Himalaya, and has been associated with modern topographic development (e.g., Wobus et al., 2006; see Fig. 2c).

A ramp in the MHT is also a feature of many structural reconstructions throughout the Himalaya, though the geophysically determined location in central Nepal is further north than

\* Corresponding author. Tel.: +1 650 724 0461.

E-mail address: warrenc@stanford.edu (W.B. Caldwell).

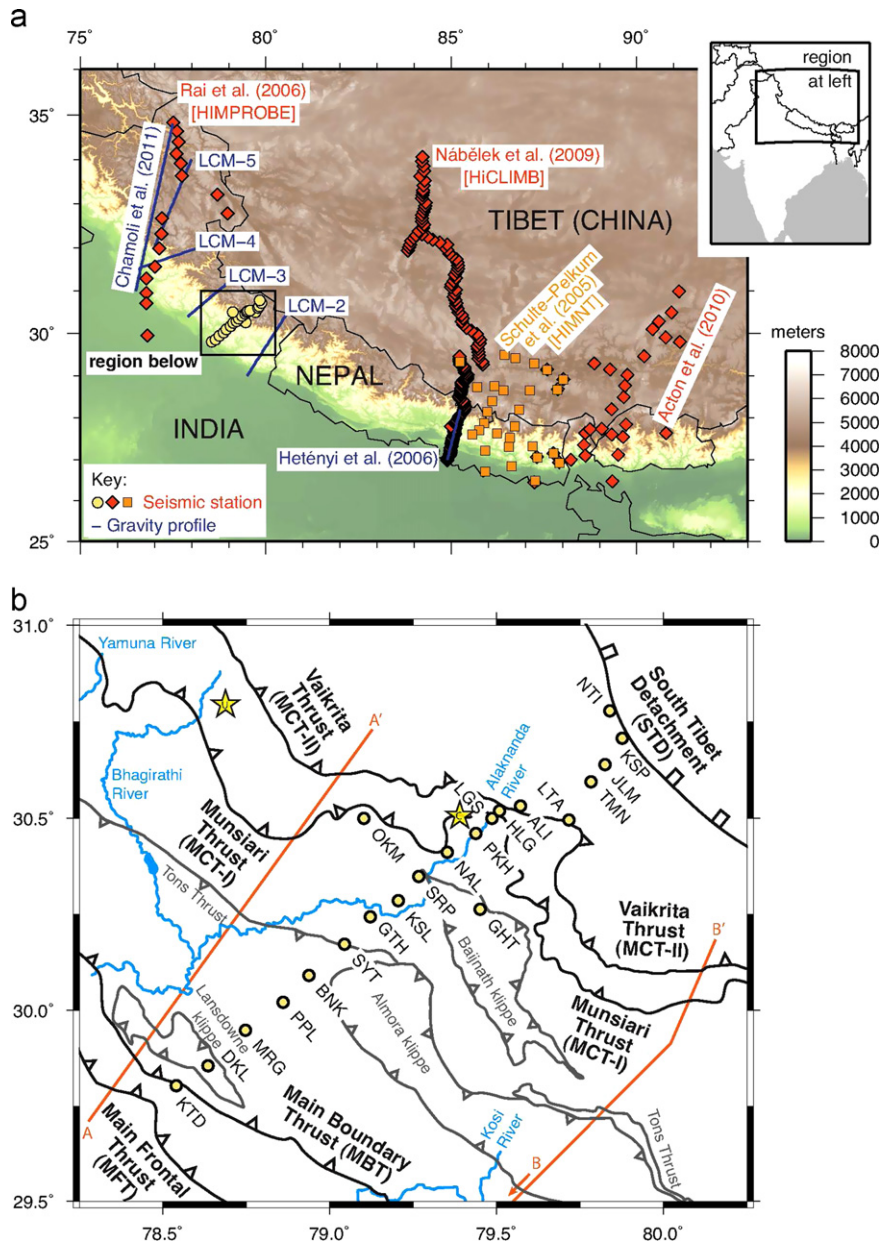


**Fig. 1.** (a) Locations of selected broadband seismic and gravity transect in the Himalaya, with experiment names (in brackets) and references (LCM signifies Lyon-Caen and Molnar, 1985). The 21-station seismic array used in this paper is shown in circles, in the boxed region that also indicates the region shown in Figs. 1b and 4b. (b) Location of broadband seismic stations used in this study in relation to major Himalayan faults. Location of STD from Yin (2006). All other faults and features adapted from Célérier et al. (2009). The klippen are sheets of GHC and thus their bounding faults correlate with the Main Central Thrust (MCT). Lines A–A' and B–B' indicate the locations of structural cross-sections shown in Fig. 2a and b. Stars are the epicenters of the 1999 Chamoli earthquake of  $M_w$  6.6 (C) and 1991 Uttarkashi  $M_w$  6.8 (U).

that determined by geologic mapping and structural data in Garhwal (Srivastava and Mitra, 1994), western Nepal (DeCelles et al., 2001; Robinson et al., 2006), central Nepal (Pearson and DeCelles, 2005; Khanal and Robinson, in review), and eastern Nepal (Schelling and Arita, 1991) (Fig. 3a). These structural cross-sections all show the MHT ramp beneath the north flank of the Almora, Dadeldhura and Kathmandhu klippen and synclinoria. Although the position of the ramp in these balanced cross-sections has been chosen to explain the locally steep dips on the north flank of the Almora, Dadeldhura, and Kathmandhu klippen and synclinoria, these cross-sections are typically drawn—within the range of admissible solutions—to provide minimum shortening estimates (Srivastava and Mitra, 1994; Robinson et al., 2006; Khanal and

Robinson, in review). In contrast, an analogous balanced cross section in the NW Himalaya places the ramp further north beneath the Munsiri Thrust/MCT-I (Webb et al., 2011).

The location and geometry of the ramp are important for characterizing earthquake hazard and understanding the nucleation of great earthquakes in the Himalaya (Pandey et al., 1995; Bilham et al., 2001), because the mid-crustal ramp is likely a focusing point for stress accumulation in the India-Asia collision (Pandey et al., 1995), which is released in great earthquakes ( $M > 8.0$ ) along the Himalayan arc (Ni and Barazangi, 1984; Bilham, 2004). These massive earthquakes rupture the MHT and, since the Pliocene, propagate to the surface at the MFT (Wesnosky et al., 1999; Avouac, 2007).

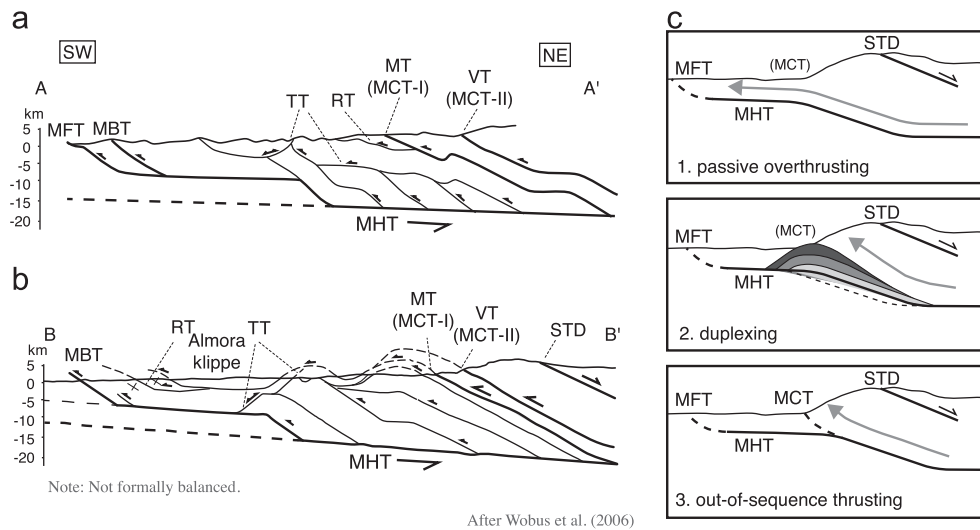


**Fig. 2.** Structural cross-sections (no vertical exaggeration) in the Garhwal Himalaya re-drawn from (a) *Srivastava and Mitra (1994)* and (b) *C  l  rier et al. (2009)* (for locations see Fig. 1b). RT=Ramgarh Thrust, TT=Tons Thrust, MT=Munsiari Thrust (MCT-I), VT=Vaikrita Thrust (MCT-II); other abbreviations as in Fig. 1b. (c) Schematic cross-sections illustrating three proposed models of Himalayan neotectonics relating focused uplift and subsequent rise of high topography to a mid-crustal ramp in the MHT: (1) passive overthrusting (e.g., *Avouac, 2007*), (2) duplexing, i.e., accretion of Indian plate material into the hanging wall of the thrust (e.g., *Bollinger et al., 2006*), (3) active, out-of-sequence thrusting at the MCT (e.g., *Wobus et al., 2006*).

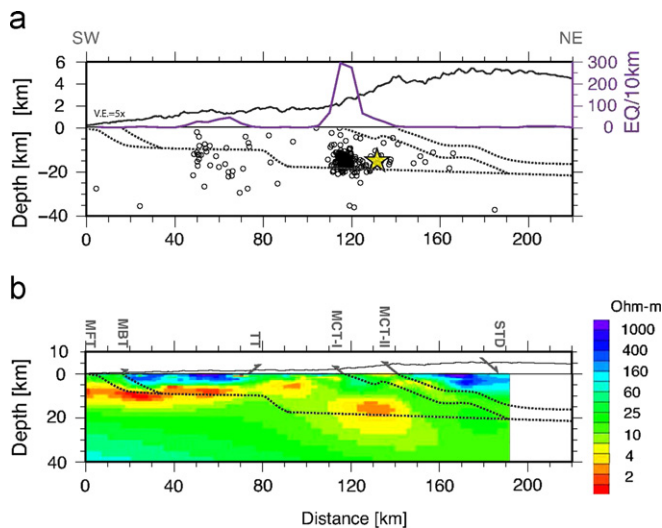


**Fig. 3.** Structural interpretation of the major Himalayan thrust faults in Garhwal (gray dotted lines) (from *Srivastava and Mitra, 1994*) projected into the line of our section, overlaid on: (a) hypocenters of local seismicity (circles) (*Mahesh et al., 2013*) and the 1999  $M_w$  6.6 Chamoli earthquake (star) and (b) electrical conductivity along our profile (*Rawat and Arora, in preparation*). Local seismicity located by *Mahesh et al. (2013)* shows locations of micro-earthquakes from 2005 to 2008 within 40 km of the profile and located with station coverage having an azimuthal gap of  $< 180^\circ$ . Also shown is a histogram of these events (number of earthquakes per 10 km cross-strike bin).

The mid-crustal ramp would be paralleled by the Moho if the Indian crust maintained constant thickness during subduction. Some seismic images from the Himalaya have been inferred to show the Moho deepening smoothly from  $\sim 40$  km beneath the Sub-Himalaya to  $\sim 70$ – $80$  km beneath the southern Tibetan plateau (e.g., *Schulte-Pelkum et al., 2005*; *N  b  lek et al., 2009*; locations of these studies shown in Fig. 1a). However, other seismic studies comment on locally steep Moho dips beneath the Higher Himalaya (*Molnar, 1988*; *Acton et al., 2010*). Furthermore, gravity transects across the Himalaya show high gradients in the Bouguer anomaly, on the order of 1.5 mGal/km in the

Garhwal Himalaya (*Lyon-Caen and Molnar, 1985*), with similar gradients also observed in the NW Himalaya (*Chamoli et al., 2011*), and central Nepal (*Het  nyi et al., 2006*) (locations of these studies shown in Fig. 1a). These gravity observations are best fit by models in which the Moho (and by inference the Indian plate) dips at  $3^\circ$  or less beneath the Lower Himalaya and  $10$ – $22^\circ$  beneath the Higher Himalaya (*Lyon-Caen and Molnar, 1985*; *Het  nyi et al., 2006*; *Chamoli et al., 2011*).

The Himalaya exhibit along-strike variations in geology, structure, geomorphology, and climate, the modeling of which requires geological and geophysical investigations beyond the heavily studied transects in central Nepal. Contributing to this effort, our study provides new geometric constraints on the subsurface structure of the Garhwal Himalaya. In this paper, we seismically image the Moho and MHT bounding the subducting Indian plate in a transect across the Garhwal Himalaya, and relate this image to the seismicity, geomorphology, and tectonics of the orogen.

### 1.1. Geologic setting

The Garhwal Himalaya span approximately  $77$ – $81^\circ\text{E}$  (*Yin, 2006*) and are drained by the Yamuna, Bhagirathi and Alaknanda rivers (Fig. 1b). The term Kumaon (or Kumaun) is also sometimes used for this region, and/or for the region immediately east. The region has seen numerous geologic studies (*Heim and Gansser, 1936*; *Valdiya, 1980*; *Srivastava and Mitra, 1994*; *C  l  rier et al., 2009*), but relatively little geophysical investigation compared to further east, in Nepal. Notably, it was in Garhwal that *Heim and Gansser (1936)* defined the classic stratigraphic sequence now recognized throughout the Himalaya: Siwalik Group (Sub-Himalaya), Lesser Himalayan Sequence (LHS), Greater Himalayan Crystallines (GHC), and Tethyan Himalayan Sequence (THS). Each of these groups is bounded to the south by a major north-dipping fault: respectively, the Main Frontal Thrust (MFT), Main Boundary Thrust (MBT), Main Central Thrust (MCT) and South Tibet Detachment (STD) (cf. *Yin, 2006*) (Fig. 1b). These faults generally young to the south, consistent with the classic model of a foreland-propagating thrust sequence (e.g., *DeCelles et al., 2001*). The LHS is further subdivided into the Mesoproterozoic Outer LHS and Neoproterozoic Inner LHS, the former carried southwest over the latter in Garhwal along the Tons Thrust (TT) which was

subsequently rotated to its current southwest dip by deeper thrust horses (C  lerier et al., 2009). The Lower and Higher Himalaya, defined topographically and separated by a physiographic break in slope, correspond approximately to the LHS and the GHC (Yin, 2006).

The Main Central Thrust (MCT) is a crustal-scale south-vergent thrust fault and zone of high ductile strain (cf. Searle et al., 2008). The upper boundary of this zone, sometimes called the MCT-II (Arita, 1983), is known locally in Garhwal as the Vaikrita Thrust (Valdiya, 1980). The lower boundary of this zone, correspondingly called the MCT-I, is known locally in Garhwal as the Munsiri Thrust, and in other parts of the Himalaya as the Almora thrust, Mahabharat thrust, or Dadelhura thrust (Searle et al., 2008). In Garhwal, the Munsiri Thrust/MCT-I places the highly metamorphosed rocks of the GHC over the metasedimentary rocks of the LHS (C  lerier et al., 2009). Observations in Garhwal of discontinuous exhumation cooling ages (Vannay et al., 2004) suggest that the Munsiri Thrust/MCT-I was active later than the Vaikrita Thrust/MCT-II (though similar observations in central Nepal have been fit by models of passive overthrusting without an active MCT-I, e.g., Robert et al., 2011).

The major thrust faults of the Himalayan system (MFT, MBT, MCT), once thought to independently cut the entire crust, are now widely accepted to root into a basal detachment termed the Main Himalayan Thrust (MHT) (e.g., Yin, 2006; Avouac, 2007) (Fig. 2a and b). The MHT is thus the detachment between the base of the Himalayan thrust wedge and the top of the subducting Indian plate. Initially proposed in geologic cross sections (Schelling and Arita, 1991; Srivastava and Mitra, 1994), the MHT is now believed to connect with a major shallow-dipping reflector observed beneath the Tethyan Himalaya in wide-angle and near-vertical seismic reflection studies at  $\sim 88\text{--}90^\circ\text{E}$  (Hirn and Sapin, 1984; Zhao et al., 1993; Makovsky et al., 1999).

In the Lower Himalaya of Garhwal, structural reconstructions interpret the MHT as having a flat-ramp-flat geometry (Srivastava and Mitra, 1994; C  lerier et al., 2009) (see Fig. 2a and b, but note that the cross section of C  lerier et al., 2009 is not formally balanced). In these cross sections, the Main Frontal Thrust cuts down from the surface to a depth of 6–8 km below sea level, and is linked by a geometric flat (dipping NE  $2\text{--}5^\circ$ ) that extends 30–50 km northward to a geometric ramp (dipping  $30\text{--}40^\circ$ ) that cuts down to 15–17 km below sea level, connecting to a deeper flat. The ramp has been located beneath the northern flank of the Almora klippe and the surface trace of the Tons thrust (Srivastava and Mitra, 1994). South of the ramp, the MHT places Neoproterozoic Outer Lesser Himalayan sequence metasedimentary rocks over  $\sim 1.5$  km of Cretaceous to Miocene continental margin and syn-orogenic clastics that in turn overlie mesoproterozoic Inner Lesser Himalayan sequence metasedimentary rocks (Srivastava and Mitra, 1994; Robinson et al., 2006). North of the ramp the MHT places Berinag orthoquartzites (Inner Lesser Himalayan sequence) over Ramgarh schists (Indian cratonic basement) (C  lerier et al., 2009; Robinson et al., 2006).

## 1.2. Neotectonic setting

The ramp in the MHT is believed to strongly control deformation in the Himalaya. Proposed mechanisms for deformation at the MHT ramp include: (1) passive overthrusting (Fig. 2c, part 1), in which movement on the MFT absorbs most of the present-day shortening across the Himalaya (e.g., Lav   and Avouac, 2001); (2) underplating at the ramp (Fig. 2c, part 2), a variation of passive overthrusting in which Indian crust from the footwall of the MHT forms duplexes which are accreted into the Himalayan wedge (Schelling and Arita, 1991; Bollinger et al., 2006); and (3) active or recently active out-of-sequence thrusting on the MCT (Fig. 2c,

part 3), possibly resulting from, or amplified by, focused erosion at the range front (e.g., Harrison et al., 1997; Wobus et al., 2003). Observations of a break in continuity in thermochronologic ages across the MCT have been argued to provide evidence for out-of-sequence thrusting (e.g., Wobus et al., 2006), although others have inferred continuity in ages across the MCT and thus argued against active out-of-sequence thrusting (e.g., Robert et al., 2009), or modeled discontinuous cooling ages with the duplex model (e.g., Bollinger et al., 2006). Thus, present thermochronological data cannot currently distinguish between these mechanisms (Herman et al., 2010). Some geodetic arguments favor the duplexing model (Fig. 2b) (Grandin et al., 2012).

Local seismic activity in Garhwal (Fig. 3a) includes two moderate-sized earthquakes in the last two decades (epicentral locations in Fig. 1b): the  $M_w$ 6.8 Uttarkashi earthquake of October 20, 1991 (Kayal, 1996) and the  $M_w$ 6.6 Chamoli earthquake of March 28, 1999 (Kayal et al., 2003) (the latter partially motivated the deployment of the seismic array used in this paper). Based on the focal depth (21 km), the shallow dip angle, and the predominant thrust motion, the Chamoli earthquake is believed to have

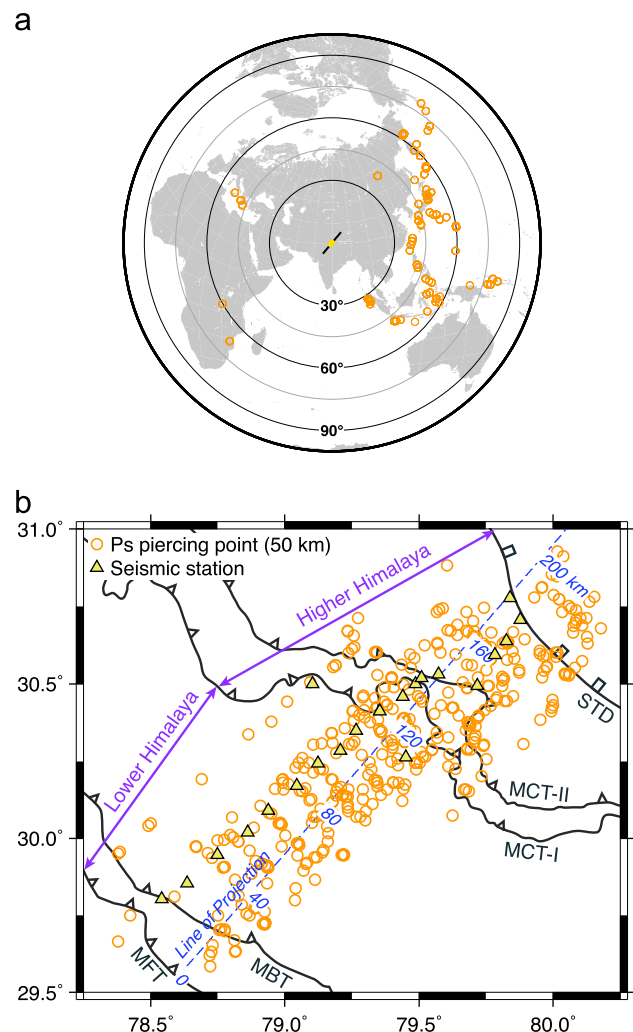


**Fig. 4.** (a) Locations of events used to calculate receiver functions. The 85 events had  $M_w > 5.5$  and epicentral distance  $30\text{--}90^\circ$ . Black line shows orientation of array. (b) Locations of piercing points of teleseismic rays (at 50 km depth), overlaid with seismic station locations and line of projection for receiver function CCP stack. Only piercing points for receiver functions used in the CCP stack are shown. Indicated distances along the profile are measured from the smoothed location of the MFT, and correspond to the horizontal scale in subsequent figures.

ruptured a small segment of the MHT (Kayal et al., 2003), whereas the Uttarkashi earthquake occurred above the detachment (Kayal, 1996). Both aftershock sequences occurred on local thrust faults south of the MCT and were distributed from the surface to the depth of the main shock.

## 2. Seismic array and data

India's National Geophysical Research Institute (NGRI) operated 21 three-component broadband seismic stations for 21 months in 2005–2006 in a line trending SW–NE in the Alaknanda River valley (Ashish et al., 2009; Mahesh et al., 2012, 2013) (station locations given in Supplementary Material, Table S1). The array was designed to study the seismotectonic setting of the damaging 1999 Chamoli earthquake (Figs. 1b and 3a), as well as the larger-scale structure of the Himalayan orogen. The southernmost station was located approximately at the surface trace of the Main Boundary Thrust, and the northernmost station was located approximately at the surface trace of the South Tibet Detachment (Fig. 1b).

The seismometers were Guralp CMG-3T or CMG-3ESP sensors recording at 40 Hz. Fifteen of the stations were deployed in a straight line, but road locations forced four of the northern stations (LTA, TMN, JLM, KSP) to be laterally offset from the rest of the line by  $\sim 20$  km (Fig. 1b). Two additional stations (OKM, GHT) located near the surface expression of the Munsiri Thrust were offset laterally by  $\sim 30$  km. The average spacing between stations

on the line was  $\sim 10$  km. Prior to this deployment, no dense broadband seismic array had been deployed in the Garhwal region.

## 3. Receiver function methodology

### 3.1. Receiver function calculation

We calculate  $P_s$  receiver functions for 245 events in our catalog with  $M_w \geq 5.5$  and epicentral distance  $30\text{--}90^\circ$  (locations of events shown in Fig. 4a and local piercing points shown in Fig. 4b). First, we isolate the incident and converted waves by rotating the seismograms from their original N-E-Z components into R-T-Z components based on the event backazimuth. Next, an automated quality-control filter rejects candidate events with poor signal-to-noise ratio. The signal-to-noise ratio is given by  $(S_{max} - S_{min}) / (N_{max} - N_{min})$ , where  $S$  is the amplitude of the signal after event arrival, and  $N$  is the amplitude of the signal prior to event arrival. We then deconvolve the radial component from the vertical component using iterative time-domain deconvolution, yielding an estimated receiver function (Gurrola et al., 1995; Ligorria and Ammon, 1999). This estimated receiver function is evaluated at each iteration by convolving it with the recorded vertical data, giving an estimate of the horizontal data, which is compared against the recorded horizontal data using an RMS misfit. Events with poor misfit are discarded.

We used a smoothly tapered high-cut Gaussian filter to remove high-frequency noise. We calculated two sets of receiver functions

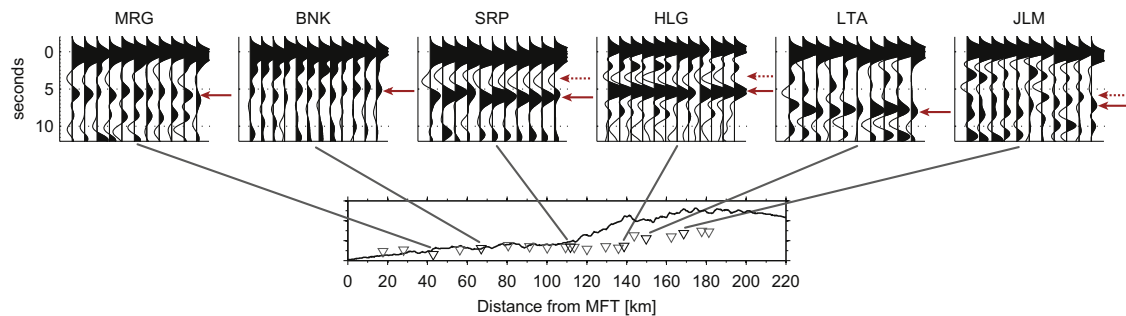


**Fig. 5.** Sample receiver functions at selected stations. The Moho appears as a prominent conversion (solid arrows) at  $\sim 6$  s beneath the Lower Himalaya (stations MRG, BNK, SRP, HLG) and deepens abruptly beneath the Higher Himalaya (station LTA). Shallower conversions at SRP and HLG (dotted arrows) are interpreted as being from the MHT. Further north, the Moho becomes less well-resolved (station JLM), in some receiver functions appearing as a double conversion (dotted arrow), suggesting the presence of fast lower-crustal material.

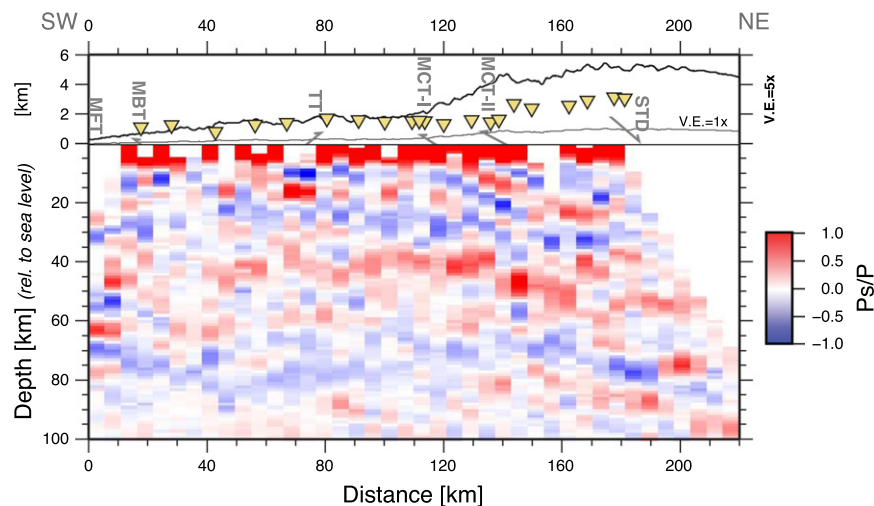


**Fig. 6.** Minimally processed, “raw” CCP stack, with no bootstrapping, smoothing, or interpolation. Bin size shown is actual bin size used for CCP stacking (1 km vertically, 5 km horizontally). Amplitudes are normalized fractions of the magnitude of the incident  $P$ -wave for each receiver function.

for two different Gaussian filter widths, low-pass filtering with a smooth roll off at 0.5 Hz for one set and 1.2 Hz for a second set. We use the lower-frequency set ( $< 0.5$  Hz) for unstacked 1-D receiver functions at individual stations (Fig. 5), and the higher-frequency set ( $< 1.2$  Hz) for 2-D CCP stacks (Figs. 6 and 7). The 1.2 Hz cut-off yields higher-resolution receiver functions than those with 0.5 Hz cut-off, with the trade-off of increased noise and ringing (which is controlled in the CCP stack better than in the unstacked receiver functions).

We then perform a manual quality-control step, viewing the receiver functions grouped by event, then grouped by station, each time discarding poor-quality events and anomalous receiver functions on the basis of visual inspection. After this step, one station (TMN) had few usable receiver functions and was ignored in subsequent analyses. Of the 20 remaining stations, seven recorded 50 or more high-quality receiver functions, and eight more recorded 35 or more high-quality receiver functions. In the end, 85 events of the 245 that were recorded yielded receiver functions of sufficient quality to be used for our analyses. In total, there were 1025 receiver functions in the lower-frequency ( $< 0.5$  Hz) set and 787 in the higher-frequency ( $< 1.2$  Hz) set.

### 3.2. CCP stacking

We use the common conversion point (CCP) stacking method (Dueker and Sheehan, 1997) to coherently stack phase conversions

(and partially cancel random noise), creating a 2-D image of impedance contrasts at depth (Figs. 6 and 7). CCP stacking has previously been utilized in the Himalaya by Schulte-Pelkum et al. (2005), using the HIMNT array, Nábělek et al. (2009), using the HiCLIMB array, and Acton et al. (2010) (locations of these arrays shown in Fig. 1a).

Two-dimensional CCP stacks are constructed by back-projecting each receiver-function time series to its appropriate spatial location in depth using ray theory and an assumed Earth velocity model (density of back-projected rays per bin shown in Supplemental Material, Figure S1). We use ray theory to calculate the full source-to-receiver path for back projection (rather than linear back-projection, which becomes increasingly inaccurate at greater depths). The values of the receiver-function time series are then binned, stacked, and normalized by  $n^{0.75}$ , where  $n$  is the number of traces per bin (noise-free signals scale by  $n$  and pure noise scales by  $n^{0.5}$ , so we use an intermediate value). The bin size of our model is 1 km vertically by 5 km horizontally. Our final stack (Fig. 7) has 15 km horizontal smoothing and 5:1 horizontal interpolation (see Supplemental Material, Figure S2). Depth is referenced to sea level (i.e., we account for topography), so dips and absolute positions of subsurface features are visually maintained, but crustal thickness is the sum of the plotted depth plus local topography.

The velocity model used for CCP back projection is based on the *iasp91* Earth velocity model (Kennett and Engdahl, 1991),

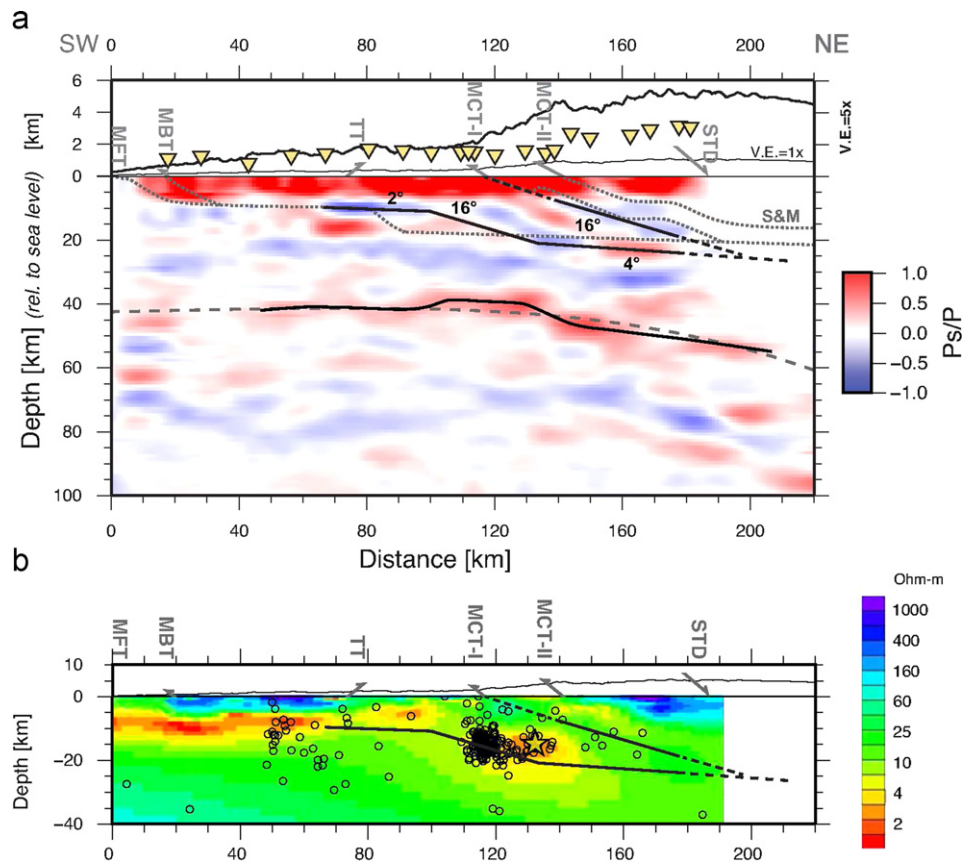


**Fig. 7.** (a) Ninety-five percent-confidence common conversion point (CCP) stack of receiver functions, at true scale (horizontal=vertical), with 15 km horizontal smoothing. Red indicates positive impedance contrast (velocity increasing downwards); amplitudes are normalized fractions of the magnitude of the incident  $P$ -wave for each receiver function. Two possible interpretations for the geometry of the Moho and MHT are given by: (i) solid black lines (dashed where uncertain) showing our preferred interpretation and (ii) dotted gray lines indicating the structural reconstruction for the MHT and MCT from a nearby geologic transect projected onto our section (S&M, Srivastava and Mitra, 1994), and a dashed gray line for the Moho derived from the calculated deflection for a flexed beam. At top, average topography along our section (bold line) and elevation of stations (which were located in valleys and do not align with average topography), shown at five times vertical exaggeration (topographic profile also shown at no vertical exaggeration, thinner line). Fault abbreviations as in Figs. 1 and 2. (b) Hypocenters of local seismicity (black circles) and the 1999  $M_w$  6.6 Chamoli earthquake (star) overlaid on our preferred interpretation of the MHT. Background is the resistivity along our section, from Rawat and Arora (in preparation).

modified at crustal depths as follows: 5.25 km/s above the MHT (0–10 km), 6.5 km/s in the middle crust (10–25 km), and 7 km/s in the lower crust (25–40 km). These values are based on published work in the western Himalaya (Rai et al., 2006; Oreshin et al., 2008; Rajendra Prasad et al., 2011; Mahesh et al., 2013) (we test variations to this model in Supplementary Material, Figure S3). We use a  $V_p/V_s$  ratio of 1.73 for the entire crust (we test the effects of different values in Supplementary Material, Figure S4).

The 2-D stacking procedure requires a choice of profile orientation. Two logical choices of orientation are (1) in line with the array, N50°E and (2) perpendicular to the approximate strike of local Himalayan structures, roughly N40°E. We use the latter in Figs. 6 and 7 (we test the effects of stacking along different orientations in Supplementary Material, Figure S5).

### 3.3. Resolution and uncertainty

Vertical resolution in 1-D receiver functions is approximately half the wavelength of the converted wave, a relationship determined empirically with both synthetic data (Bostock and Rondenay, 1999) and field data (Rychert et al., 2007). Our receiver functions are low-pass filtered, so the highest frequency, and hence maximum resolution, is set by the filter cut-offs ( $\sim 0.5$  Hz for the 1-D receiver functions and  $\sim 1.2$  Hz for the 2-D CCP stack, see Section 3.1). These correspond to, respectively, wavelengths of 8 km and 3.3 km for a lower-crustal velocity of  $V_s = 4.0$  km/s. Halving these wavelengths gives the nominal vertical resolution at the Moho: 4 km for the 1-D receiver functions, and 1.7 km for the CCP stack.

Lateral resolution for CCP stacking is determined by the Fresnel zone of the converted wave (Rondenay, 2009). Zhai and Levander (2011) determine that in order to successfully image structure that varies along the section, Fresnel zones must overlap by  $\sim 50\%$  or more at the depth of interest. The Fresnel zone width for  $P_s$  at 40 km depth is  $\sim 40$  km, so our station spacing of  $\sim 10$  km yields 75% overlap at that depth, sufficient to image the Moho well. At 10 km depth, the Fresnel zone width is  $\sim 20$  km, so our station spacing yields 50% overlap at that depth, leading to image degradation at depths shallower than 10 km.

We use bootstrapping to help constrain the uncertainty that results from variations and noise in the receiver functions. We ran 30 realizations of the CCP stack with families of receiver functions randomly selected from the full pool (with duplication, so that the number of receiver functions for each realization was the same as the number of unique receiver functions). From these realizations we calculated the mean and standard deviation ( $\sigma$ ) of the values in each bin of the image, and prior to geological interpretation we discarded bins with mean amplitudes less than  $2\sigma/n^{0.5}$ . Thus only values greater than  $2\sigma$  are in the final image (Fig. 7), meaning we have 95% confidence that the values shown represent the real Earth. Of the 4141 bins in the image,  $\sim 730$  had a normalized mean below  $2\sigma$ , and were set to zero prior to smoothing (see Supplementary Material, Figures S2B and S2C). Fig. 6 shows the minimally processed CCP stack without bootstrapping and subsequent masking of poorly constrained bins.

Velocity differences between the model used for back projection and the real Earth present another source of uncertainty. If receiver functions are back projected in a velocity model faster than the real Earth, conversions will appear too deep; if the velocity model is slower than the real Earth, conversions will appear too shallow. To constrain the depth uncertainty in the CCP stack resulting from error in the velocity model, we back projected and stacked using two additional velocity models, one 5% faster throughout the crust relative to our preferred model (described in Section 3.2), and one 5% slower (tests shown in

Supplementary Material, Figure S3). We observe that the Moho in the 5% fast model is 2–4 km deeper than in the 5% slow model (the shift in Moho depth is not by a constant amount throughout the image because different velocity models cause receiver functions with different ray parameters to be binned and stacked differently). In other words, a  $\sim 10\%$  change in the velocity model yields a 5–10% change in the depth of the Moho. It is unlikely that our preferred velocity model is in error by a full 10% throughout the entire crust, so this test provides an upper bound on this source of error.

A 1-D velocity model does not account for lateral velocity variation, leading to further differences between model velocities and Earth velocities. Two known sources of laterally varying velocity in the Himalaya are (1) the northward-deepening Moho, which will make average lithospheric velocities slower as the Moho deepens to the north, and an opposite effect, (2) the general northward increase in metamorphic grade between the LHS and GHC, which will make average crustal velocities faster as the metamorphic grade increases to the north. Because these two effects are of opposite sign, they will partially cancel. We quantify the effect of (1) by performing a CCP stack using a velocity model with the Moho at 60 km depth, which ensures that all Moho conversions are back-projected using crustal velocities (using our preferred velocity model with a 40-km-deep Moho, conversions from Moho depths greater than 40 km will be partially back projected using mantle velocities). In the resulting CCP stack, the conversions seen in Fig. 7 at 50–55 km depth, 170 km north of the MFT appeared shallower by  $< 2$  km. Thus, for our preferred model, this effect may lead to a slight over-prediction of Moho depth north of 160 km. The effect of (2) will be of opposite sign, and can be bounded using the observation that a 10% decrease in velocity for the entire crust makes the Moho appear shallower by 2–4 km (see above). The actual effect of (2) will be smaller, since changes in metamorphic grade will not affect the entire crust. We conclude that these two sources of error, which have opposite sign and magnitude on the order of our resolution, are not likely to significantly compromise our image.

A 1-D velocity model also fails to account for any lateral variation in  $V_p/V_s$  ratio. Nábělek et al. (2009) observe a significant cross-strike change in  $V_p/V_s$  in the Himalaya, from 1.85 beneath the Sub-Himalaya to 1.6 beneath the Higher Himalaya. We generate CCP stacks using velocity models with these two  $V_p/V_s$  ratios, and observe that Moho conversions are 4–6 km (10–15%) deeper with  $V_p/V_s = 1.6$  than with  $V_p/V_s = 1.85$  (Supplementary Material, Figure S4). Thus variations in the  $V_p/V_s$  ratio have a bigger influence on back-projected depths than absolute changes in velocity. The trend identified by Nábělek et al. (2009) would tend to remove the visual suggestion of a slight southward dip to our Moho image beneath the Lesser Himalaya, and make the Moho beneath the Greater Himalaya dip more steeply than shown in Fig. 7.

## 4. Results

In the 1-D receiver functions, the Moho creates a strong positive conversion at  $\sim 6$  s beneath the Lesser Himalaya, deepening to  $\sim 8$  s beneath the Higher Himalaya and becoming less distinct further north (Fig. 5). At the northern end of the profile (e.g., JLM), the Moho signature is complex, appearing in many of the receiver functions as a double conversion. This could indicate the presence of high velocity lower crustal material, which has been observed elsewhere in the Himalaya and interpreted and modeled as eclogite (Schulte-Pelkum et al., 2005; Hetényi et al., 2007). Upper-crustal conversions are clear at the stations beneath the Lower Himalaya (e.g., BNK, HLG).

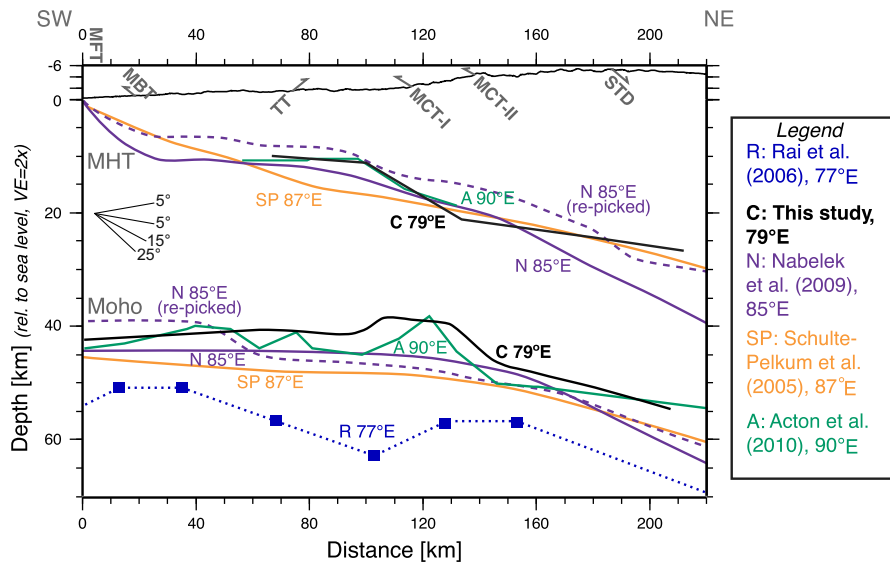


**Fig. 8.** Our Moho and MHT picks for Garwhal, as in Fig. 7, compared with the locations of features inferred in other receiver function studies throughout the Himalaya (all use receiver function CCP stacking, except for the 1-D receiver function study of Rai et al. (2006), which also locates only the Moho). Locations of these studies shown in Fig. 1a, and their approximate longitudes indicated in this figure. Topography and fault traces are for Garwhal. Other cross sections aligned using the MBT and MCT as references. For Nábělek et al. (2009), solid lines indicate their inferred structure, while the dashed lines are our picks of the relevant features in their CCP stack.

In the 2-D CCP stack (Figs. 6 and 7), the Moho appears as a strong, continuous conversion throughout the central portion of the array, where the ray coverage is most dense. At the edges of the model, particularly at the northern end, the image is less well-constrained, and the Moho appears weaker (though this may also be an effect of lower-crustal high-velocity material).

Beneath the Sub-Himalaya and Lower Himalaya, the Moho is 35–45 km deep, and appears nearly horizontal, or even dipping slightly southward (the apparent southward dip, which is contrary to a simple model of uniform Indian crust subducting beneath a northward-thickening Himalayan thrust wedge, could be due to depth projection errors resulting from a northward decrease in  $V_p/V_s$  ratio, as discussed in Section 3.3, or to a real change in the thickness of subducted Indian crust).

Beneath the Higher Himalaya, the peak positive amplitude assumed to be the Moho conversion abruptly deepens by 5 km, 135–140 km north of the MFT (Fig. 7), representing a local dip of 15–30°. The Moho conversion is less continuous at 160–210 km north of the MFT, and at 195 km three positive conversions of similar amplitude appear at 37, 52, and 75 km depth below sea-level. The conversion at 52 km depth is our preferred interpretation for the Moho, as it creates the smoothest Moho profile and is consistent with the depths determined in other studies (Fig. 8). Although an abrupt deepening of the Moho to 75 km depth cannot be ruled out from the receiver functions alone, and might correspond to the steeply dipping Moho beneath the Higher Himalaya inferred in gravity models (17°: Lyon-Caen and Molnar, 1985, 18°: Chamoli et al., 2011), this would be deeper than previously reported Moho depths beneath the Tethyan Himalaya (Hirn and Sapin, 1984; Zhao et al., 1993; Nábělek et al., 2009), and would imply significant northward thickening of subducted Indian crust.

If the Moho is at 50 km depth (or more) 160–200 km north of the MFT, then the positive conversion at 37 km is in the lower crust (cf. similar image of Schulte-Pelkum et al., 2005). This downwards transition to higher velocities would be expected of eclogite, as discussed above, and, if present, this high-velocity lower-crustal material could account for the reduction in Moho

amplitude at the northern end of the profile (cf. Nábělek et al., 2009).

The upper crust exhibits a negative–positive (blue-over-red) doublet, from roughly 70 km north of the MFT (starting at ~10 km depth) to roughly 125 km north of the MFT, and again at 140 km north of the MFT to 180 km north of the MFT (Fig. 7). We interpret this as the complex response to the various lithologies juxtaposed by the MHT and MCT, discussed in detail in Section 5.1. These conversions appear in the 1-D receiver functions in the Lower Himalaya (Fig. 5) and span the depths in which previous cross-sections place the MHT and MCT (Fig. 8).

A discontinuous positive conversion appears in the CCP stack at 65 km depth beneath the Lower Himalaya, shallowing to 55 km beneath the Higher Himalaya. This conversion is likely a crustal multiple (cf. Schulte-Pelkum et al., 2005).

## 5. Discussion

### 5.1. MHT depth and polarity

The seismic signature of a fault depends largely on the lithologies juxtaposed across it. Thrust faults commonly place older, deeply exhumed rocks above younger, shallower rocks. Because deeply buried rocks generally have higher seismic wave-speeds and densities than shallower rocks (assuming similar lithologies), the simplest expectation for seismic images of thrust faults is that of a negative impedance contrast—that is, the product of velocity and density decreases with depth (blue in our CCP section). This appears true for the MHT from 65 to 105 km north of the MFT, where Proterozoic metasedimentary rocks (Outer Lesser Himalaya sequence) overlie a kilometer-thick layer of Tertiary fluvial syn-orogenic deposits (Srivastava and Mitra, 1994; Robinson et al., 2006) of presumably significantly lower seismic velocities. Elevated electrical conductivities suggest that water is trapped at or below the MHT in this region (Fig. 3) (Rawat, 2012; Rawat and Arora, in preparation), further lowering seismic velocities below the detachment and thereby enhancing

the negative impedance contrast. Below the MHT, and below the thin Tertiary sequence, a  $\sim 7$  km Proterozoic metasedimentary sequence (Inner Lesser Himalaya) with Berinag orthoquartzites at the base overlies Indian cratonic basement (Ramgarh Group of C  lerier et al., 2009), likely creating a positive seismic-impedance contrast. We therefore interpret the blue-over-red (negative-over-positive) pair of seismic converters with respective depths  $\sim 10$  km and  $\sim 16$  km, from 65 to 105 km north of the MFT (Fig. 7) as the MHT and top of Indian basement, respectively. (Our ability to measure the precise depths to the MHT is contingent upon our inference that the MHT is represented by the peak negative amplitude, and is limited by the finite wavelength of our data.)

Where the MHT steepens at the mid-crustal ramp inferred in structural cross-sections, the Tertiary rocks are cut out of the section, and the ramp places Inner Lesser Himalaya sequence over Inner Lesser Himalaya sequence (C  lerier et al., 2009; Robinson et al., 2006). The basal unit of the overlying Inner Lesser Himalaya sequence is the Berinag orthoquartzite, whereas rocks immediately below the MHT ramp include significant amounts of carbonates, a juxtaposition which should exhibit a velocity increase downward (Christensen and Mooney, 1995), and hence a positive (red) seismic impedance contrast for the ramp. We thus interpret the weak positive (red) converter that extends from  $\sim 12$  km depth, 105 km north of the MFT to  $\sim 18$  km depth, 125 km north of the MFT as representing the ramp in the detachment. Although dipping structures can be problematic to image with receiver functions, they are best imaged when the backazimuth of the sources coincides with the direction of dip and, consequently, the incident *P*-waves impinge obliquely on the dipping interface (Cassidy, 1992; N  b  lek et al., 2009). Fortunately then for our analysis, the azimuthal distribution of events is predominantly from the northeast (Fig. 4a), giving us the optimal configuration for imaging a northeast-dipping ramp in the MHT. To further constrain the dip and position of the ramp, we note that the ramp must connect the upper ( $\sim 10$  km depth) and lower ( $\sim 20$  km depth; see following paragraph) flats of the MHT over a distance of 25–35 km. This constrains the dip of the ramp to be in the range of 10–25 $^\circ$ ; our preferred interpretation is of a dip of 16 $^\circ$ .

The flat north of the ramp, extending from 130 km north of the MFT to the branch line of the MCT and MHT ( $\sim 200$  km north of the MFT) places Inner Lesser Himalaya sequence over Indian basement, and we would anticipate a positive impedance contrast. However, this is true only in the absence of confounding factors such as crustal fluids. The magnetotelluric profile coincident with our seismic profile finds its highest conductances in this portion of the profile, with resistivities below 3  $\Omega$  m between  $\sim 15$  and 20 km depth 120 and 140 km north of the MFT (Fig. 7b) (Rawat, 2012; Rawat and Arora, in preparation). Those values can only sensibly be explained by the presence of free aqueous fluids, which strongly lower seismic velocities. Because these fluids are likely trapped beneath the detachment, we anticipate a velocity decrease downwards, and therefore interpret the MHT as passing through the negative (blue) conversion in our CCP section, 135–150 km north of the MFT (further discussed below in Section 5.2). Between 155 and 180 km north of the MFT, resistivities return to average, and we infer the MHT as creating a positive (red) impedance contrast, consistent with the expected lithologies. North of the MCT branch line ( $\sim 200$  km north of the MFT), the MHT should juxtapose crystalline gneisses of the GHC above Indian cratonic basement, and we therefore cannot easily predict seismic polarity based on lithology; furthermore, at this location we lose resolution in our image. Further east (86–91 $^\circ$ E), previous direct observations of the MHT at wide-angle (Hirn and Sapin, 1984; Makovsky et al., 1999; Zhang and Klemperer, 2010) find a

positive impedance contrast north of the surface trace of the STD, in a structural location where melts appear to be common above the MHT along the entire arc of the Himalaya (Unsworth et al., 2005; Caldwell et al., 2009).

The Munsiri Thrust/MCT-I places Indian basement above Inner Lesser Himalaya sequence (Srivastava and Mitra, 1994; C  lerier et al., 2009), and we therefore anticipate a negative impedance contrast, and interpret the negative (blue) converter that projects to the surface close to the trace of the Munsiri Thrust and Vaikrita Thrust (Fig. 7) as representing the Munsiri Thrust/MCT-I. Dips between 12 $^\circ$  and 32 $^\circ$  can fit this conversion, though our preferred interpretation is of a 16 $^\circ$  dip, parallel to the MHT ramp.

In our preferred interpretation (solid lines in Fig. 7a), we draw the ramp in the MHT dipping northeast at 16 $^\circ$ , and positioned to give the simplest structure consistent with our expectations for the seismic polarity of the MHT and MCT. The deeper flat best fits our CCP image if it dips 4 $^\circ$  NE. We cannot rule out more complex structures with multiple smaller ramps below the limit of our resolution, but a single major ramp in the MHT adequately fits the data. We place this ramp 20–30 km north of the previous interpretation of Srivastava and Mitra (1994), and with vertical relief of  $\sim 10$  km, similar to previous proposals. Although we show a significantly gentler dip ( $\sim 16^\circ$ ) than previous interpretations (30–40 $^\circ$  of Srivastava and Mitra, 1994), this may be due to the horizontal smoothing applied (unsmoothed images allow dips as large as 25 $^\circ$ , see Fig. 6). The more northerly position for the ramp compared to that of Srivastava and Mitra (1994) is predicated on the assumption that the negative (blue) conversion at  $\sim 10$  km depth beneath the Lower Himalaya represents the MHT as far north as 105 km north of the MFT. Although construction of a revised balanced cross-section is beyond the scope of this paper, we note that significant revisions to the thrust-belt architecture of Srivastava and Mitra (1994), which would change their cross-section, have been proposed by C  lerier et al. (2009). For example, C  lerier et al. show the Tons Thrust as older than and cut by the MCT, and as juxtaposing Outer Lesser Himalayan sequence with Greater Himalayan Crystallines, as opposed to Srivastava and Mitra (1994), who show the Tons Thrust as part of the duplex system of the Inner Lesser Himalayan sequence beneath the MCT. Additionally, Srivastava and Mitra (1994) re-interpreted the Berinag Thrust (Valdiya, 1980; C  lerier et al., 2009) as having purely normal motion. We also note that new studies along our seismic profile—using orogen-perpendicular changes in river steepness, elevation, relief, and annual precipitation—identify a geomorphic boundary, and, by implication, the up-dip limit of the mid-crustal ramp, in the same position as we interpret from our seismic image (Morell et al., 2012). Morell et al. suggest that their neotectonic observations are best explained by duplex accretion along the mid-crustal ramp (Fig. 2c, part 2), as preferred by us from our seismic images of the MHT and Moho (see Section 5.5).

These interpretations for the MHT and MCT-I are shown as solid black lines in Fig. 7 (dashed where less certain). We compare them with the MHT and MCT-I from the nearest balanced structural cross-section (Y–Y' of Srivastava and Mitra, 1994, shown as a dotted gray line in Fig. 7), rotated into the line of our section and stretched so the surface traces of the MFT and MCT-I match those of our profile. The negative–positive pair we interpret as the MHT and top of Indian basement contact dip 2 $^\circ$  northeast, and fit the structural cross section within methodological uncertainty, given that our seismic wavelengths are comparable with the spacing of key impedance contrasts in the metasedimentary section (so the peak amplitude on our CCP image may not correspond precisely with depth to the converter). Where the MHT shallows (between 0 and 55 km north of

the MFT) any conversion from the MHT is obscured by interference with the direct arrival in the receiver functions.

### 5.2. MHT ramp, seismicity, and free fluids

From 130 to 150 km north of the MFT, we infer a negative polarity for the MHT, as discussed in Section 5.1. This polarity is not predicted by the lithology contrasts in the cross-sections of Srivastava and Mitra (1994) or C  lerier et al. (2009). However, additional constraints are provided by new broadband magnetotelluric data (along a profile approximately collinear with our seismic profile) which have been inverted for electrical conductivities down to 40 km depth, from south of the MFT to the STD (Rawat, 2012; Rawat and Arora, in preparation) (Figs. 3b and 7b). Regions of shallow high conductivity observed in these sections are presumably related to connate water in the Ganges Basin south of the MFT, and to water trapped in underthrust sediments beneath the Lesser Himalayan thrust sheet as far north as 100 km north of the MFT. From 100 to 110 km north of the MFT, the magnetotelluric inversion shows a clear break in the conductor, coincident with where we interpret a positive impedance contrast on a ramp in the MHT (Fig. 7b). However, north of the ramp, the highest conductances on the profile (on the order of 3000 S, with local peak conductivities of  $> 0.33$  S/m) occur between 125 and 145 km north of the MFT at depths of 12 and 20 km. These high conductivities at modest depths in an active subduction system, in which underthrust cold surface rocks lower the geothermal gradient, can only plausibly be the result of free water in the upper crust. Similar inferences have been made from analogous conductivity observations 100 km west in Uttarakhand (Israil et al., 2008) and 500 km east in central Nepal (Lemonnier et al., 1999).

The center of this region of enhanced electrical conductivity lies directly over the region of negative polarity in our interpreted MHT, and we infer that water released by metamorphic dehydration reactions in the subducting Indian basement is trapped beneath the MHT in this location, leading to a velocity inversion and negative impedance contrast. Tomographic inversions for seismic velocity using the abundant local microseismicity also indicate low  $V_p$  and high  $V_p/V_s$  in this region (Mukhopadhyay and Kayal, 2003; Mahesh et al., 2012), consistent with our inference of the presence of free water. Measurements of the seismic attenuation of the intra-crustal shear and higher-mode surface wave phase Lg show an order of magnitude increase in attenuation at about 120 km north of the MFT on our profile (Ashish et al., 2009). We associate this attenuation with the upper-crustal fluids, and infer that the attenuation is related to free water. Local seismicity recorded by our array in 2005–2006 and a subsequent sparser areal array in 2006–2008 (Mahesh et al., 2013) was concentrated at a mean depth of 15 km just north of the surface projection of the Munsiri Thrust/MCT-I (Figs. 3a and 7b), up-dip of the negative-polarity segment of the MHT, and overlapping with our inferred ramp (though we cannot know if this spatial distribution of seismicity reflects the long term trend). Whereas Pandey et al. (1995) inferred the ramp location in central Nepal from the locus of peak microseismicity, in Garhwal our CCP profile provides independent imaging of the ramp overlapping the highest concentration of seismicity.

The aseismic nature of the negative-polarity segment of the MHT is consistent with the presence of fluids, since free fluids promote the transition from brittle faulting to stable sliding (Avouac, 2003). This location could thus also mark the locking line of the MHT in Garhwal—up-dip, the fault is locked and strain from subduction is released seismically, and down-dip, the presence of fluids and higher temperatures promotes creeping behavior on the detachment. The concentration of local seismicity

at this location is consistent with this interpretation, as stress accumulation focuses microseismic activity at the down-dip edge of locked faults (Bollinger et al., 2004). Thus we propose that the locking line of the MHT in Garhwal may be located 130 km north of the MFT, at 20 km depth (approximately below the surface trace of the Munsiri Thrust/MCT-I), where the positive impedance contrast of the MHT becomes negative and down-dip of where seismicity is concentrated.

### 5.3. Moho depth

We present two possible interpretations of the depth of the Moho in our CCP image. The first traces as strictly as possible the peak positive amplitudes of the conversion (black line in Fig. 7). This is almost certainly over-interpreting the results of an imperfect method operating on imperfect data; nevertheless, if taken at face value, it implies topography of up to 5 km on the Moho, as well as a thickness of subducted Indian crust between the MHT and Moho that varies between 20 and 28 km, with the thickness actually increasing down dip in the center of the profile. This runs counter to the simple expectation of constant thickness of subducting crust, and, if not in part an artifact of mislocated energy (which may be possible given the 1-D velocity model used for back projection), implies that either the Indian crust varied in thickness before subduction or that it has been subjected to irregular deformation patterns since subduction. A second interpretation (dashed gray line in Fig. 7) shows a smooth curve calculated using the equation for the flexure of a beam fixed at one end and subjected to a line load and a bending moment (Turcotte and Schubert, 2002), with reasonable parameter values tuned to give a good visual fit to the peak positive amplitude. This interpretation provides the smoothest possible Moho profile, with no local topography. Whereas the strict picking of peak amplitudes probably over-interprets certain features of the image, this smooth curve probably ignores some meaningful variations.

### 5.4. Comparison to similar studies throughout the Himalaya

In Fig. 8, we compare our interpreted MHT and Moho structures with those proposed from other receiver-function studies. Although the different interpretations broadly overlap in depth, we show more structural detail and infer a more complex polarity structure than previously reported.

In central Nepal, N  b  lek et al. (2009) interpret a continuous negative conversion as the MHT between the MBT and the Lhasa terrane, north of the Yarlung Zangbo suture, citing: (1) the Tertiary sedimentary rocks directly beneath the MHT, north of the ramp (e.g., Robinson et al., 2006) and (2) the possible presence of water trapped beneath the MHT (and, at greater depths further north, the presence of partial melts). An approximately collinear magnetotelluric profile does show localized low electrical resistivity beneath the MFT and MBT, and also near the transition from the Lower to the Higher Himalaya (Lemonnier et al., 1999), supporting the presence of fluids, but, as in our profile, the high conductivities are not continuous down dip. Additionally, magnetotelluric and seismic data suggest that partial melts in the Himalayan mid-crust are above, not below, the MHT (Unsworth et al., 2005; Caldwell et al., 2009). We therefore suggest that important structural and tectonic details may be lost in the schematic cross-section of N  b  lek et al. (2009), which depicts the MHT as a smoothly dipping negative conversion continuous for 400 km across strike. We also note that a positive conversion in the CCP section of N  b  lek et al. (2009) occurs at the same depth and position as the positive conversion in our CCP section, and a shallower, negative conversion of similar amplitude, which they interpret the MHT, is likewise present in our image.

The occurrence of a negative–positive doublet in approximately the same position in both CCP sections may indicate similarity in the impedance character of the MHT along strike, despite varied interpretations.

Other observations in central Nepal suggest that the impedance contrast of the MHT is controlled by anisotropic velocities in a sheared layer surrounding the detachment (Schulte-Pelkum et al., 2005). The anisotropic shear zone observed in that work has no net amplitude above 15 km in the CCP stack, suggesting no difference in average velocity above and below the detachment. This anisotropic shear zone and a 17–20 km deep converter merge at 20 km depth and have the same polarity as the Moho, indicating that beneath the Greater Himalaya, the MHT exhibits a velocity increase downwards.

In Sikkim, Acton et al. (2010) also image a negative–positive doublet, possibly showing a ramp, though they interpret and draw the MHT as the zero-crossing between the two peak amplitudes that projects northward to the MHT imaged in reflection studies (Zhao et al., 1993).

Given the complexity of the thrust sheets on vertical scales less than typical CCP imaging resolution, the imaged converters must be a low-pass representation of the allochthonous and sub-thrust autochthonous Lesser Himalayan sedimentary rocks above the Indian basement. Any more detailed seismic interpretation will require higher frequency data coupled with petrophysical measurements of Himalayan rocks to inform detailed waveform modeling.

The Moho in Garwhal from our CCP section is shallower by an average of 10–25 km than to the west in the NW Himalaya (Rai et al., 2006), and 0–10 km shallower than to the east in central Nepal and Sikkim (Nábělek et al., 2009; Schulte-Pelkum et al., 2005; Acton et al., 2010) (Fig. 8). We interpret these differences as reflecting along-strike variation in the type and thickness of crust subducted beneath the Himalaya, inferred by projecting exposures of the Paleoproterozoic and Archean cratons of India across the 200–400 km width of the Gangetic Basin (Meert et al., 2010) along the NNE convergence direction of India with Asia (015–020°: e.g., Avouac, 2007). Crust entering the subduction zone of the NW Himalaya along the line of the Rai et al. (2006) study is presumed to be Paleoproterozoic Aravalli fold belt and overlying Neoproterozoic Marwar Supergroup (Meert et al., 2010). Although stations on the exposed craton show crustal thickness of ~37 km (Vijay Kumar et al., 2012), the significantly thicker crust seen in receiver functions just south and north of the MFT (Rai et al., 2006) is confirmed by seismic reflection data that show a c. 45 km basement thickness. These depths have been used to argue for a Paleoproterozoic Wangtu-Ulleri crustal thickening event in this region (Rajendra Prasad et al., 2011). East of our study area, crust entering the subduction zone of central and eastern Nepal is presumed to be Proterozoic Vindhyan Basin, exposure of which has crustal thicknesses of ~44 km (Vijay Kumar et al., 2012). Crust entering the subduction zone of the Garwhal Himalaya is presumed to be the thinner Archean Bundelkhand shield, ~38 km thick (Vijay Kumar et al., 2012). Thus the relatively shallow Moho we image compared to profiles to the northwest and east may be an indication of subduction of Archean rather than Proterozoic basement beneath the Garwhal Himalaya.

### 5.5. Neotectonic thrust style

Our CCP image does not directly distinguish between models of Himalayan neotectonics: our imaging of the Munsiri Thrust cannot test whether it is active as an out-of-sequence thrust (Fig. 2c, part 3), as our interpreted image is adequately explained by the lithologic contrasts that may have been emplaced in the Miocene, as in the passive overthrusting or duplexing models

(Fig. 2c, parts 1 & 2). However, the relative Moho and MHT geometries may bear on these mechanisms. We observe a Moho depth of 42 km at the MFT, comprising ~28 km Indian cratonic basement, ~8 km Inner Lesser Himalayan sequence, and ~6 km Gangetic basin (syn-orogenic sediments). The same ~28 km of basement is still present at the up-dip (southerly) limit of the ramp (100 km north of the MFT), but has decreased to ~20 km only 30 km NE at the down-dip (northerly) limit of the ramp (130 km north of the MFT), based on our preferred interpretations (solid lines in Fig. 7). This rapid thinning can only be avoided with a substantially different Moho geometry that is not represented by the high amplitude converters at 40–50 km depth, 110–160 km north of the MFT. Even though these Moho conversions have some uncertainty in depth due to uncertainty in crustal velocities, our uncertainty tests—see Section 3.3 and Supplemental Material, Figures S3 & S4—indicate that even an incorrect velocity model would not account for 8 km of error in Moho depth. If the substantial crustal thinning from 100 to 130 km north of the MFT is an inherited feature of the Indian crust, then we are observing the Himalaya at a unique time in its development. If instead we regard the Himalaya as in approximately steady-state, then if Indian crust is being passively overthrust by the Himalayan thrust sheets (Fig. 2c, part 1), this thinning could be achieved by extreme ductile thinning in the lower cratonic crust (the upper crust is brittle here, as shown by the seismicity, Fig. 3). More plausibly, duplexing intermittently removes the top part of the subducting basement, incorporating it into the upper plate (Fig. 2c, part 2). Application of this test elsewhere in the Himalaya requires collocated high-resolution imaging of the Moho and MHT. Although Nábělek et al. (2009) and Schulte-Pelkum et al. (2005) choose to draw smoothed interpretations of the Moho and MHT in their schematic cross-sections, which ignore significant variability in their published CCP images, Acton et al. (2010), like us, interpret substantial thinning of the Indian basement beneath their MHT ramps (Fig. 8), which we believe is similarly suggestive of duplexing.

## 6. Conclusions

Our observations place spatial constraints on the geometry of the Moho and Main Himalayan Thrust (MHT) in the Garwhal Himalaya. Our receiver-function imaging captures an approximately horizontal Moho at 35–45 km depth below sea level beneath the Lower Himalaya which deepens to at least 50–55 km beneath the Higher Himalaya. This Moho depth is at a similar depth or up to 10 km shallower than that observed in central Nepal, and 10–25 km shallower than in the NW Indian Himalaya, implying an along-strike variation in the thickness of pre-subduction Indian crust: the observed thickness of subducted Indian crust between the MHT and the Moho is 20–28 km in Garwhal, possibly indicating subduction of a thin Archean craton at this longitude. The down-dip thinning of subducted Indian crust is consistent with the underplating/duplexing model of Himalayan neotectonics.

We image the MHT as having a complex polarity signature and a flat–ramp–flat geometry (though we cannot interpret structural relationships directly from our seismic section, and thus our application of the terms *ramp* and *flat* to features in our image is based on correlating observed impedance contrasts with lithologic juxtapositions in published cross sections, and not an assertion that the MHT necessarily cuts structurally up-section or along-section, as in the strict geologic definitions of these terms). The MFT and MBT cut down from the surface to meet the upper flat of the MHT at depths too shallow for us to image. This upper flat is imaged in our CCP section and has a negative impedance contrast and dips north at 2° at 10–17 km depth beneath the

Lesser Himalaya. A velocity decrease with depth is consistent with the juxtaposition of rock types across the MHT in Garhwal, as inferred from geologic mapping and structural cross sections.

A ramp occurs in the MHT between 100 and 130 km north of the MFT, and the MHT depth changes from  $\sim 10$  km below sea level to  $\sim 20$  km below sea level. The geometric constraints imposed by the need to link the upper and lower flats constrains the dip of the ramp to be in the range of  $10\text{--}25^\circ$ ; our preferred interpretation is a dip of  $16^\circ$ . The impedance contrast of this ramp is positive, consistent with expected geology. Because our seismic image is most simply fit by a single ramp with the same vertical dimension as published balanced cross-sections ( $\sim 7\text{--}8$  km), we suggest that there is only a single large ramp beneath the Himalaya, vertically beneath the Munsiri Thrust/MCT-I, at the physiographic transition from the Lesser to the Higher Himalaya. This ramp is 20–30 km north of that inferred by the only existing structural reconstruction in Garhwal (Srivastava and Mitra, 1994). Our interpretation is predicated on a continuous negative amplitude conversion on the upper flat of the MHT. Such a ramp has been shown in numerical models to strongly control kinematics and exhumation patterns in the Himalaya (Bollinger et al., 2006; Herman et al., 2010; Robert et al., 2011).

The deeper flat in the MHT that lies north of the ramp, between 130 and 190 km north of the MFT, has a negative impedance contrast for 20–30 km, starting 10 km north of the surface location of the Munsiri Thrust/MCT-I, down-dip of the mid-crustal ramp and beneath the surface trace of the MCT-II. This segment coincides with a peak in electrical conductivity ( $> 0.3$  S/m) and is down-dip of a peak in microseismicity, suggesting the presence of fluids trapped below the detachment.

## Acknowledgments

All seismic data were acquired with equipment and funding of the National Geophysical Research Institute (NGRI) Hyderabad, India. Analysis and interpretation were funded by Stanford University and NSF Continental Dynamics EAR 0409939. We thank G. Rawat, B. Arora, and S. Khanal for providing their results prior to publication, J.P. Avouac for a review of an earlier version of this paper, and D. Robinson and P. DeCelles for helpful discussions of their balanced cross-sections.

## Appendix A. Supplementary materials

Supplementary data associated with this article can be found in the online version at <http://dx.doi.org/10.1016/j.epsl.2013.02.009>.

These data include a Google Earth KML file with the locations of the seismic stations used in this paper.

## References

- Acton, C.E., Priestley, K., Mitra, S., Gaur, V.K., 2010. Crustal structure of the Darjeeling–Sikkim Himalaya and southern Tibet. *Geophys. J. Int.* 184 (2), 829–852, URL <http://dx.doi.org/10.1111/j.1365-246X.2010.04868.x>.
- Arita, K., 1983. Origin of the inverted metamorphism of the lower Himalayas, Central Nepal. *Tectonophysics* 95 (1–2), 43–60. URL <http://www.sciencedirect.com/science/article/pii/0040195183902585>.
- Ashish, Padhi, A., Rai, S.S., Gupta, S., 2009. Seismological evidence for shallow crustal melt beneath the Garhwal High Himalaya, India: implications for the Himalayan channel flow. *Geophys. J. Int.* 177 (3), 1111–1120, URL <http://dx.doi.org/10.1111/j.1365-246X.2009.04112.x>.
- Avouac, J.-P., 2003. Mountain building, erosion, and the seismic cycle in the Nepal Himalaya. In: *Advances in Geophysics*, vol. 46. Elsevier, pp. 1–80. URL <http://www.sciencedirect.com/science/article/B7RNH-4G1N8C-2/2/bfd87637bcfa431c6c91428cba6567e5>.
- Avouac, J.-P., 2007. Dynamic processes in extensional and compressional settings—mountain building: from earthquakes to geological deformation. In: Schubert, G. (Ed.), *Treatise on Geophysics*. Elsevier, Amsterdam, pp. 377–439. URL

- <http://www.sciencedirect.com/science/article/B8STY-4PT21S9-3F2/f11f4a4b1abc169263acac460c894fe4>.
- Berger, A., Jouanne, F., Hassani, R., Mugnier, J.L., 2004. Modelling the spatial distribution of present-day deformation in Nepal: How cylindrical is the Main Himalayan Thrust in Nepal?. *Geophys. J. Int.* 156 (1), 94–114, URL <http://dx.doi.org/10.1111/j.1365-246X.2004.02038.x>.
- Bilham, R., 2004. Earthquakes in India and the Himalaya: tectonics, geodesy and history. *Ann. Geophys.* 47 (2–3), 839–858. URL <http://www.annalsofgeophysics.eu/index.php/annals/article/view/3338>.
- Bilham, R., Gaur, V.K., Molnar, P., 2001. Himalayan seismic hazard. *Science* 293 (5534), 1442–1444. URL <http://www.sciencemag.org/content/293/5534/1442.short>.
- Bollinger, L., Avouac, J.P., Cattin, R., Pandey, M.R., 2004. Stress buildup in the Himalaya. *J. Geophys. Res.* 109 (November (B11)), B11405, URL <http://dx.doi.org/10.1029/2003JB002911>.
- Bollinger, L., Henry, P., Avouac, J., 2006. Mountain building in the Nepal Himalaya: thermal and kinematic model. *Earth Planet. Sci. Lett.* 244 (1–2), 58–71. URL <http://www.sciencedirect.com/science/article/pii/S0012821X06000859>.
- Bostock, M.G., Rondenay, S., 1999. Migration of scattered teleseismic body waves. *Geophys. J. Int.* 137 (June (3)), 732–746. URL <http://www.blackwell-synergy.com/doi/abs/10.1046/j.1365-246X.1999.00813.x>.
- Caldwell, W.B., Klempere, S.L., Rai, S.S., Lawrence, J.F., 2009. Partial melt in the upper-middle crust of the northwest Himalaya revealed by Rayleigh wave dispersion. *Tectonophysics* 477 (November (1–2)), 58–65. URL <http://www.sciencedirect.com/science/article/B6V72-4VDS88C-1/2/f53902ad014517ed983c721a191f0f0e>.
- Cassidy, J.F., 1992. Numerical experiments in broadband receiver function analysis. *Bull. Seismol. Soc. Am.* 82 (3), 1453–1474. URL <http://www.bssaonline.org/content/82/3/1453>.
- Chamoli, A., Pandey, A., Dimri, V., Banerjee, P., 2011. Crustal configuration of the northwest Himalaya based on modeling of gravity data. *Pure Appl. Geophys.* 168, 827–844, URL <http://dx.doi.org/10.1007/s00024-010-0149-2>.
- Christensen, N.I., Mooney, W.D., 1995. Seismic velocity structure and composition of the continental crust: a global view. *J. Geophys. Res.* 100 (B6), 9761–9788. URL <http://www.agu.org/pubs/crossref/1995/95JB00259.shtml>.
- Célerier, J., Harrison, T.M., Webb, A.A.G., Yin, A., 2009. The Kumaun and Garhwal Lesser Himalaya, India: Part 1. Structure and stratigraphy. *Geol. Soc. Am. Bull.* 121 (9–10), 1262–1280. URL <http://gsabulletin.gsapubs.org/cgi/content/abstract/121/9-10/1262>.
- DeCelles, P.G., Robinson, D.M., Quade, J., Ojha, T.P., Garzzone, C.N., Copeland, P., Upreti, B.N., 2001. Stratigraphy, structure, and tectonic evolution of the Himalayan fold-thrust belt in western Nepal. *Tectonics* 20 (4), 487–509. URL <http://www.agu.org/journals/ABS/2001/2000TC001226.shtml>.
- Dueker, K.G., Sheehan, A.F., 1997. Mantle discontinuity structure from midpoint stacks of converted P to S waves across the Yellowstone hotspot track. *J. Geophys. Res.* 102 (B4), 8313–8327, URL <http://dx.doi.org/10.1029/96JB03857>.
- Grandin, R., Doin, M.-P., Bollinger, L., Pinel-Puysségur, B., Ducret, G., Jolivet, R., Sapkota, S.N., 2012. Long-term growth of the Himalaya inferred from interseismic InSAR measurement. *Geology*. 40, 1059–1062, <http://dx.doi.org/10.1130/G33154.1> URL <http://geology.gsapubs.org/content/early/2012/09/18/G33154.1.abstract>.
- Gurrola, H., Baker, G.E., Minster, J.B., 1995. Simultaneous time-domain deconvolution with application to the computation of receiver functions. *Geophys. J. Int.* 120 (3), 537–543, URL <http://dx.doi.org/10.1111/j.1365-246X.1995.tb01837.x>.
- Harrison, T.M., Ryerson, F., Fort, P.L., Yin, A., Lovera, O.M., Catlos, E., 1997. A Late Miocene–Pliocene origin for the Central Himalayan inverted metamorphism. *Earth Planet. Sci. Lett.* 146, E1–E7. URL <http://www.sciencedirect.com/science/article/pii/S0012821X96002154>.
- Heim, A., Gansser, A., 1936. Central Himalaya: geological observations of the Swiss Expedition 1936. *Denschr. Schweiz. Naturforsch. Ges.* 73 (1).
- Herman, F., Copeland, P., Avouac, J.-P., Bollinger, L., Mahéo, G., LeFort, P., Rai, S., Foster, D., Pécher, A., Stüwe, K., Henry, P., 2010. Exhumation, crustal deformation, and thermal structure of the Nepal Himalaya derived from the inversion of thermochronological and thermobarometric data and modeling of the topography. *J. Geophys. Res.* 115 (June (B6)), B06407, URL <http://dx.doi.org/10.1029/2008JB006126>.
- Hetényi, G., Cattin, R., Brunet, F., Bollinger, L., Vergne, J., Nábelek, J.L., Diament, M., 2007. Density distribution of the India plate beneath the Tibetan plateau: geophysical and petrological constraints on the kinetics of lower-crustal eclogitization. *Earth Planet. Sci. Lett.* 264 (1–2), 226–244. URL <http://www.sciencedirect.com/science/article/B6V61-4PV2S31-1/2/8f573dc01cd9c0c28b6cd0951a83e46>.
- Hetényi, G., Cattin, R., Vergne, J., Nábelek, J.L., 2006. The effective elastic thickness of the India Plate from receiver function imaging, gravity anomalies and thermomechanical modelling. *Geophys. J. Int.* 167 (3), 1106–1118, URL <http://dx.doi.org/10.1111/j.1365-246X.2006.03198.x>.
- Hirn, A., Sapin, M., 1984. The Himalayan zone of crustal interaction—suggestions from explosion seismology. *Ann. Geophys.* 2 (2), 123–130.
- Israil, M., Tyagi, D., Gupta, P., Niwas, S., 2008. Magnetotelluric investigations for imaging electrical structure of Garhwal Himalayan corridor, Uttarakhand, India. *J. Earth Syst. Sci.* 117, 189–200, URL <http://dx.doi.org/10.1007/s12040-008-0023-0>.
- Kayal, J.R., 1996. Precursor seismicity foreshocks and aftershocks of the Uttarkashi earthquake of October 20, 1991 at Garhwal Himalaya. *Tectonophysics* 263 (October (1–4)), 339–345. URL <http://www.sciencedirect.com/science/article/B6V72-3VVT59G-1D/2/d0beeeaa3e7749a9a5d832ad516189c2>.
- Kayal, J.R., Ram, S., Singh, O.P., Chakraborty, P.K., Karunakar, G., 2003. Aftershocks of the March 1999 Chamoli earthquake and seismotectonic structure of the

- Garhwal Himalaya. *Bull. Seismol. Soc. Am.* 93 (1), 109–117. URL <http://www.bssaonline.org/cgi/content/abstract/93/1/109>.
- Kennett, B.L.N., Engdahl, E.R., 1991. Traveltimes for global earthquake location and phase identification. *Geophys. J. Int.* 105 (2), 429–465. URL <http://dx.doi.org/10.1111/j.1365-246X.1991.tb06724.x>.
- Khanal, S., Robinson, D.M. Upper crustal shortening and forward modeling of the Himalayan thrust belt along the Budhi-Gandaki River, central Nepal. *Int. J. Earth. Sci.* in review.
- Kumar, S., Wesnousky, S.G., Rockwell, T.K., Briggs, R.W., Thakur, V.C., Jayangondaperumal, R., 2006. Paleoseismic evidence of great surface rupture earthquakes along the Indian Himalaya. *J. Geophys. Res.* 111 (March (B3)), B03304. URL <http://dx.doi.org/10.1029/2004JB003309>.
- Lavé, J., Avouac, J.P., 2001. Fluvial incision and tectonic uplift across the Himalayas of central Nepal. *J. Geophys. Res.* 106 (B11), 26561–26591. URL <http://dx.doi.org/10.1029/2001JB000359>.
- Lemonnier, C., Marquis, G., Perrier, F., Avouac, J.-P., Chitrakar, G., Kafle, B., Sapkota, S., Gautam, U., Tiwari, D., Bano, M., 1999. Electrical structure of the Himalaya of central Nepal: high conductivity around the mid-crustal ramp along the MHT. *Geophys. Res. Lett.* 26 (21), 3261–3264. URL <http://dx.doi.org/10.1029/1999GL008363>.
- Ligorria, J.P., Ammon, C.J., 1999. Iterative deconvolution and receiver-function estimation. *Bull. Seismol. Soc. Am.* 89 (5), 1395–1400. URL <http://www.bssaonline.org/cgi/content/abstract/89/5/1395>.
- Lyon-Caen, H., Molnar, P., 1985. Gravity anomalies, flexure of the Indian plate, and the structure, support and evolution of the Himalaya and Ganga Basin. *Tectonics* 4 (6), 513–538. URL <http://dx.doi.org/10.1029/TC004i006p00513>.
- Mahesh, P., Gupta, S., Rai, S., Sarma, P.R., 2012. Fluid driven earthquakes in the Chamoli Region, Garhwal Himalaya: evidence from local earthquake tomography. *Geophys. J. Int.* 191 (3), 1295–1304. URL <http://dx.doi.org/10.1111/j.1365-246X.2012.05672.x>.
- Mahesh, P., Rai, S.S., Sivaram, K., Paul, A., Gupta, S., Sarma, R., Gaur, V.K., 2013. One dimensional reference velocity model and precise locations of earthquake hypocenters in the Central (Kumaon-Garhwal) Himalaya. *Bull. Seismol. Soc. Am.* 103 (February (1)), 328–339. URL <http://www.bssaonline.org/content/103/1/328>.
- Makovsky, Y., Klempner, S.L., Ratschbacher, L., Alsdorf, D., 1999. Midcrustal reflector on in-depth wide-angle profiles: an ophiolitic slab beneath the India-Asia suture in southern Tibet?. *Tectonics* 18 (5), 793–808. URL <http://www.agu.org/pubs/crossref/1999/1999TC900022.shtml>.
- Meert, J.G., Pandit, M.K., Pradhan, V.R., Banks, J., Sirianni, R., Stroud, M., Newstead, B., Gifford, J., 2010. Precambrian crustal evolution of Peninsular India: a 3.0 billion year odyssey. *J. Asian Earth Sci.* 39 (6), 483–515. URL <http://www.sciencedirect.com/science/article/pii/S1367912010001574>.
- Molnar, P., 1988. A review of geophysical constraints on the deep structure of the Tibetan Plateau, the Himalaya and the Karakoram, and their tectonic implications. *Philos. Trans. R. Soc. London. Ser. A Math. Phys. Sci.* 326, 33–88.
- Morell, K.D., Sandiford, M., Rajendran, C. P., Rajendran, K., Sanwal, J., Kotlia, B., Woodhead, J., Hellstrom, J., 2012. Neotectonics of the Kumaun-Garhwal region of the Indian Himalaya. Abstract T51F-1471475. In: 2012 Fall Meeting, AGU, San Francisco, CA, 3–7 December.
- Mukhopadhyay, S., Kayal, J.R., 2003. Seismic tomography structure of the 1999 Chamoli earthquake source area in the Garhwal Himalaya. *Bull. Seismol. Soc. Am.* 93 (4), 1854–1861. URL <http://www.bssaonline.org/cgi/content/abstract/93/4/1854>.
- Ni, J., Barazangi, M., 1984. Seismotectonics of the Himalayan collision zone: geometry of the underthrusting Indian Plate beneath the Himalaya. *J. Geophys. Res.* 89 (B2), 1147–1163. URL <http://www.agu.org/pubs/crossref/1984/JB089iB02p01147.shtml>.
- Nábělek, J., Hetényi, G., Vergne, J., Sapkota, S., Kafle, B., Jiang, M., Su, H., Chen, J., Huang, B., 2009. The Hi-CLIMB Team, 2009. Underplating in the Himalaya-Tibet collision zone revealed by the Hi-CLIMB experiment. *Science* 325 (September (5946)), 1371–1374. URL <http://www.sciencemag.org/cgi/content/abstract/325/5946/1371>.
- Orshin, S., Kiselev, S., Vinnik, L., Prakasam, K.S., Rai, S.S., Makeyeva, L., Savvin, Y., 2008. Crust and mantle beneath western Himalaya, Ladakh and western Tibet from integrated seismic data. *Earth Planet. Sci. Lett.* 271 (July (1–4)), 75–87. URL <http://www.sciencedirect.com/science/article/B6V61-4S75V5W-B/1/FS096411b58e331b1080e5abc52b3e0>.
- Pandey, M.R., Tandukar, R.P., Avouac, J.P., Lavé, J., Massot, J.P., 1995. Interseismic strain accumulation on the Himalayan crustal ramp (Nepal). *Geophys. Res. Lett.* 22 (7), 751–754. URL <http://dx.doi.org/10.1029/94GL02971>.
- Pearson, O.N., DeCelles, P.G., 2005. Structural geology and regional tectonic significance of the Ramgarh thrust, Himalayan fold-thrust belt of Nepal. *Tectonics* 24 (July (4)), TC4008. URL <http://dx.doi.org/10.1029/2003TC001617>.
- Rai, S.S., Priestley, K., Gaur, V.K., Mitra, S., Singh, M.P., Searle, M., 2006. Configuration of the Indian Moho beneath the NW Himalaya and Ladakh. *Geophys. Res. Lett.* 33 (August), L15308. URL <http://www.agu.org/pubs/crossref/2006/2006GL026076.shtml>.
- Rajendra Prasad, B., Klempner, S.L., Rao, V.V., Tewari, H., Khare, P., 2011. Crustal structure beneath the Sub-Himalayan fold-thrust belt, Kangra recess, north-west India, from seismic reflection profiling: implications for Late Paleoproterozoic orogenesis and modern earthquake hazard. *Earth Planet. Sci. Lett.* 308 (1–2), 218–228. URL <http://www.sciencedirect.com/science/article/pii/S0012821X11003451>.
- Rawat, G., 2012. Electrical Conductivity Imaging of Uttarakhand Himalaya Using MT Method. Ph.D. Thesis. Indian Institute of Technology (IIT), Roorkee, India.
- Rawat, G., Arora, B.R. Electrical resistivity cross-section across the Garhwal Himalaya: Proxy to fluid-seismicity linkage. *Geophys. Res. Lett.*, in preparation.
- Robert, X., van der Beek, P., Braun, J., Perry, C., Dubille, M., Mugnier, J.-L., 2009. Assessing Quaternary reactivation of the Main Central thrust zone central Nepal Himalaya: new thermochronologic data and numerical modeling. *Geology* 37 (8), 731–734. URL <http://geology.gsapubs.org/content/37/8/731.abstract>.
- Robert, X., van der Beek, P., Braun, J., Perry, C., Mugnier, J.-L., 2011. Control of detachment geometry on lateral variations in exhumation rates in the Himalaya: insights from low-temperature thermochronology and numerical modeling. *J. Geophys. Res.* 116 (B5), B05202. URL <http://dx.doi.org/10.1029/2010JB007893>.
- Robinson, D.M., DeCelles, P.G., Copeland, P., 2006. Tectonic evolution of the Himalayan thrust belt in western Nepal: implications for channel flow models. *Geol. Soc. Am. Bull.* 118 (July (7–8)), 865–885. URL <http://gsabulletin.gsapubs.org/content/118/7-8/865>.
- Rondenay, S., 2009. Upper mantle imaging with array recordings of converted and scattered teleseismic waves. *Surv. Geophys.* 30, 377–405. URL <http://dx.doi.org/10.1007/s10712-009-9071-5>.
- Rychert, C.A., Rondenay, S., Fischer, K.M., 2007. P-to-S and S-to-P imaging of a sharp lithosphere-asthenosphere boundary beneath eastern North America. *J. Geophys. Res.* 112 (B8), B08314. URL <http://dx.doi.org/10.1029/2006JB004619>.
- Schelling, D., Arita, K., 1991. Thrust tectonics, crustal shortening, and the structure of the far-eastern Nepal Himalaya. *Tectonics* 10 (5), 851–862. URL <http://dx.doi.org/10.1029/91TC01011>.
- Schulte-Pelkum, V., Monsalve, G., Sheehan, A., Pandey, M.R., Sapkota, S., Bilham, R., Wu, F., 2005. Imaging the Indian subcontinent beneath the Himalaya. *Nature* 435 (7046), 1222–1225. URL <http://dx.doi.org/10.1038/nature03678>.
- Searle, M.P., Law, R.D., Godin, L., Larson, K.P., Streule, M.J., Cottle, J.M., Jessup, M.J., 2008. Defining the Himalayan Main Central Thrust in Nepal. *J. Geol. Soc.* 165 (March (2)), 523–534. URL <http://jgs.lyellcollection.org/cgi/content/abstract/165/2/523>.
- Srivastava, P., Mitra, G., 1994. Thrust geometries and deep structure of the outer and lesser Himalaya, Kumaun and Garhwal (India): implications for evolution of the Himalayan fold-and-thrust belt. *Tectonics* 13 (1), 89–109. URL <http://www.agu.org/pubs/crossref/1994/93TC01130.shtml>.
- Turcotte, D.L., Schubert, G., 2002. *Geodynamics*, 2nd edition Cambridge University Press.
- Unsworth, M.J., Jones, A.G., Wei, W., Marquis, G., Gokarn, S.G., Spratt, J.E., 2005. Crustal rheology of the Himalaya and southern Tibet inferred from magnetotelluric data. *Nature* 438 (7064), 78–81. URL <http://dx.doi.org/10.1038/nature04154>.
- Valdiya, K.S., 1980. *Geology of Kumaun Lesser Himalaya*. Wadia Institute of Himalayan Geology.
- Vannay, J., Grasemann, B., Rahn, M., Frank, W., Carter, A., Baudraz, V., Cosca, M., 2004. Miocene to Holocene exhumation of metamorphic crustal wedges in the NW Himalaya: evidence for tectonic extrusion coupled to fluvial erosion. *Tectonics* 23. URL <http://www.agu.org/pubs/crossref/2004/2002TC001429.shtml>.
- Vijay Kumar, T., Jagadeesh, S., Rai, S.S., 2012. Crustal structure beneath the Archean-Proterozoic terrain of north India from receiver function modeling. *Journal of Asian Earth Sciences* 58, 108–118. URL <http://dx.doi.org/10.1016/j.jseas.2012.06.015>.
- Webb, A.A.G., Yin, A., Harrison, T.M., Célérier, J., Gehrels, G.E., Manning, C.E., Grove, M., 2011. Cenozoic tectonic history of the Himachal Himalaya (northwestern India) and its constraints on the formation mechanism of the Himalayan orogen. *Geosphere* 7 (4), 1013–1061. URL <http://geosphere.gsapubs.org/content/7/4/1013.abstract>.
- Wesnousky, S.G., Kumar, S., Mohindra, R., Thakur, V.C., 1999. Uplift and convergence along the Himalayan Frontal Thrust of India. *Tectonics* 18 (6), 967–976. URL <http://dx.doi.org/10.1029/1999TC900026>.
- Wobus, C.W., Hodges, K.V., Whipple, K.X., 2003. Has focused denudation sustained active thrusting at the Himalayan topographic front? *Geology* 31 (10), 861–864. URL <http://geology.gsapubs.org/content/31/10/861.abstract>.
- Wobus, C.W., Whipple, K.X., Hodges, K.V., 2006. Neotectonics of the central Nepalese Himalaya: constraints from geomorphology, detrital 40Ar/39Ar thermochronology, and thermal modeling. *Tectonics* 25 (4), TC4011. URL <http://dx.doi.org/10.1029/2005TC001935>.
- Yin, A., 2006. Cenozoic tectonic evolution of the Himalayan orogen as constrained by along-strike variation of structural geometry, exhumation history, and foreland sedimentation. *Earth-Sci. Rev.* 76 (1–2), 1–131. URL <http://www.sciencedirect.com/science/article/B6V62-4J73052-1/2/a4d8d5af3bc7c793ae4c282603e4893d>.
- Zhai, Y., Levander, A., 2011. Receiver function imaging in strongly laterally heterogeneous crust: synthetic modeling of BOLIVAR data. *Earthquake Sci.* 24, 45–54. URL <http://dx.doi.org/10.1007/s11589-011-0768-4>.
- Zhang, Z., Klempner, S., 2010. Crustal structure of the Tethyan Himalaya, southern Tibet: new constraints from old wide-angle seismic data. *Geophys. J. Int.* 181 (3), 1247–1260. URL <http://dx.doi.org/10.1111/j.1365-246X.2010.04578.x>.
- Zhao, W., Nelson, K.D., & Project INDEPTH Team., 1993. Deep seismic reflection evidence for continental underthrusting beneath southern Tibet. *Nature* 366 (December(6455)), 557–559. URL <http://dx.doi.org/10.1038/366557a0>.

# Supplemental Material for: Characterizing the Main Himalayan Thrust in the Garhwal Himalaya, India with receiver function CCP stacking

Warren B. Caldwell, Simon L. Klemperer, Jesse F. Lawrence, Shyam S. Rai, Ashish

In preparing this work we explored a variety of parameters for processing and displaying the common conversion point (CCP) stacks. In this supplemental material we show some of our tests of these parameters. The stability and consistency of these images with respect to different stacking projections, velocity models and  $V_p/V_s$  ratios allows us to have confidence in the features of the CCP image that we choose to interpret. Fiducial lines, when shown, are always at the same fixed locations. Displacements of the Moho, Main Himalayan Thrust (MHT) and Munsiri Thrust/MCT-I converters with respect to these fiducial lines provides an estimate of uncertainty of their absolute locations.

## Ray density

The density of ray paths per bin of the model is shown in Figure S1. The angled nature of the energy is the result of the majority of events arriving from the northeast. These counts are used to normalize the CCP stack.

## Image smoothing

Published CCP images typically have some arbitrary imaging parameters applied in order to render them more amenable to visual interpretation. We illustrate the step-by-step effects of our image processing sequence in Figure S2.

## Velocity model for back projection

Back projection of the teleseismic rays requires a velocity model in order to correctly locate the receiver function energy. As described in the main text, we used a velocity model composed of values from the literature for the western Himalaya (5.25 km/s above the MHT (0–10 km), 6.5 km/s in the middle crust (10–25 km), and 7 km/s in the lower crust (25–40 km), and *iasp91* values below the 40 km-deep Moho). We tested models that were 5% slower and 5% faster throughout the crust in order to constrain how uncertainty in the Earth’s velocity will affect the accuracy of our image (Figure S3). This test shows that Moho depths were at most 2–4 km deeper when back projected with the 5% fast model than

with the 5% slow model. The effect was less for shallower features.

We also tested models with varying  $V_p/V_s$  ratio (Figure S4). Nábělek et al. (2009) observed a significant cross-strike change in  $V_p/V_s$  in central Nepal, from 1.85 beneath the Sub-Himalaya to 1.6 beneath the Higher Himalaya. We observe that Moho conversions are 4–6 km (10–15%) deeper with  $V_p/V_s = 1.6$  than with  $V_p/V_s = 1.85$ . Our 1-D velocity model cannot account for lateral variation (and has a fixed  $V_p/V_s$  ratio of 1.73), but if we did back project with the laterally-varying  $V_p/V_s$  ratio of Nábělek et al. (2009), conversions in the left half of the CCP section would shallow, and conversions in the right half would deepen, effectively increasing the northward dip of planar features.

## Orientation of line of projection

The CCP stack is a projection of rays traveling in three dimensions onto a two-dimensional plane, so the orientation of the profile influences how the data are stacked. Figure S5 shows CCP stacks (smoothed and interpolated, but without masking or bootstrapping) for profiles of varying azimuthal orientation. An orientation most in-line with the seismometer array (050°) offers the greatest coherence of stacked energy for shallow conversions, whereas an orientation orthogonal to regional orogenic structure (040° or 030°) offers the greatest stacking coherence for deeper geologic structures, since structure not orthogonal to the profile will appear smeared across bins when stacked. Consistent with this expectation, the MHT and MCT-I appear clearest when projected along 040°, while the Moho appears clearest when projected along 050° (see the sharp, well-defined, continuous contrast between the reds of the Moho conversion and the underlying blue as the Moho deepens north of kilometer 120). However, because the features are broadly similar between different profile orientations, we chose 040° as the profile orientation for the figures shown in the paper.

Latitude (°N)	Longitude (°E)	Elevation (m)	Station name
29.803	78.541	1079	KTD
29.855	78.636	1234	DKL
29.947	78.748	806	MRG
30.021	78.862	1294	PPL
30.091	78.938	1405	BNK
30.172	79.045	1681	SYT
30.243	79.123	1579	GTH
30.285	79.207	1451	KSL
30.349	79.267	1492	SRP
30.500	79.103	1525	OKM
30.263	79.452	1489	GHT
30.412	79.353	1303	NAL
30.460	79.439	1585	PKH
30.500	79.487	1448	LGS
30.519	79.509	1627	HLG
30.531	79.572	2669	ALI
30.495	79.717	2361	LTA
30.595	79.784	2541	TMN
30.639	79.825	2916	JLM
30.707	79.877	3115	KSP
30.778	79.840	3065	NTI

Table S1: Locations of broadband seismic stations.

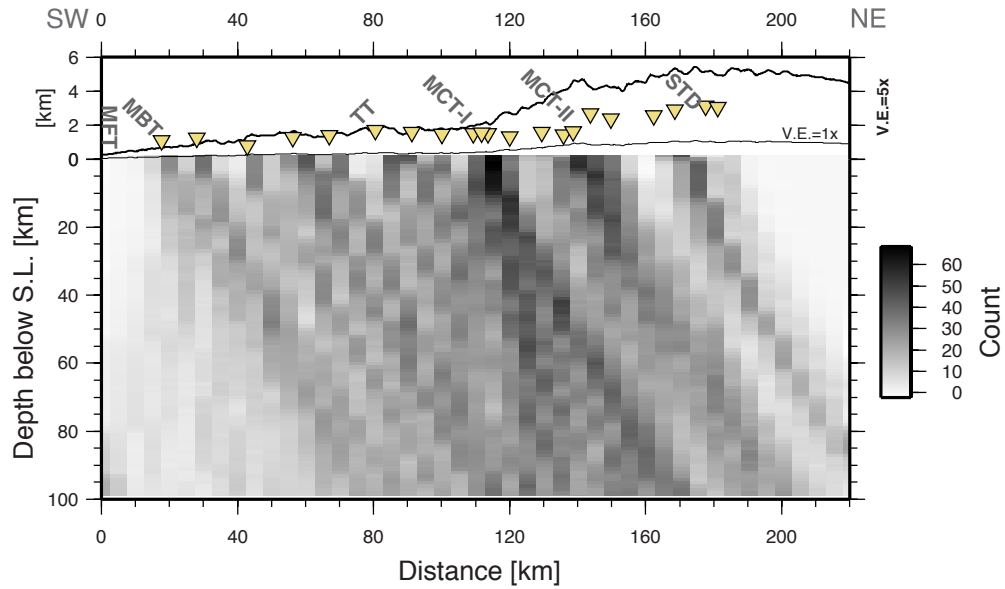


Figure S1: Number of receiver functions stacked in each bin of the CCP section.

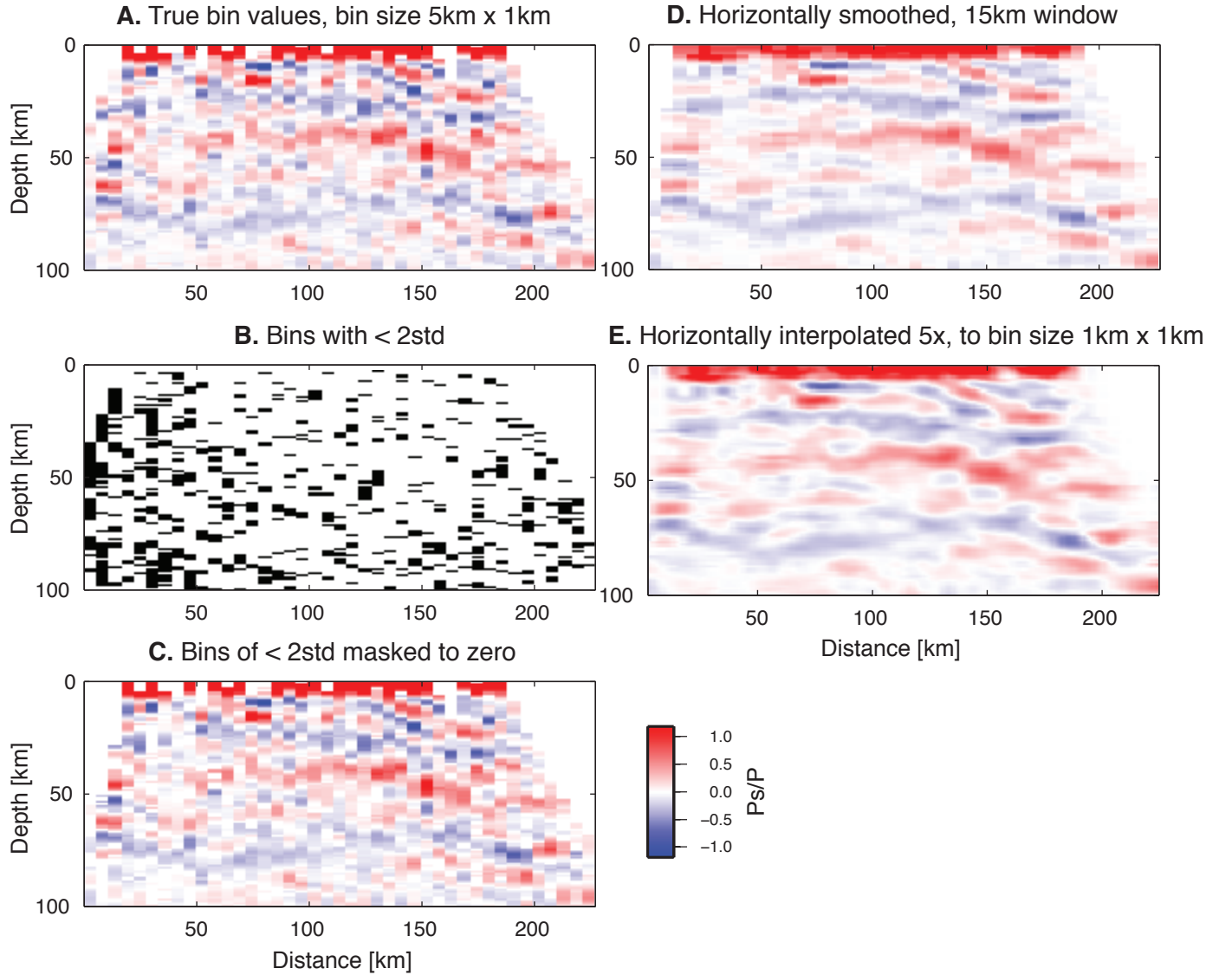


Figure S2: Image processing steps used to generate the final common conversion point (CCP) receiver function stack shown in the main text. (A) Minimally-processed, “raw” CCP stack prior to bootstrapping, smoothing, and interpolation. Bin size shown is bin size used for CCP stacking (1 km vertically, 5 km horizontally). This display of the stack is also shown in the main text in Figure 6. (B) Bins with mean amplitude less than two standard deviations (black), as determined by bootstrapping. (C) CCP stack after masking any bins for which the mean amplitude is less than two standard deviations. Values shown in this panel are therefore above the 95% confidence threshold. (D) CCP stack after applying a horizontal smoothing filter consisting of a simple 15 km rolling average. (E) CCP stack after interpolating 5x horizontally, yielding a displayed bin size of 1km x 1km. This display of the stack is shown in the main text in Figure 7. Scalebar range greater than  $\pm 1$  because the stack is normalized by  $n^{0.75}$  (where  $n$  is the count of rays per bin), as described in the main text (same scalebar for subsequent figures).

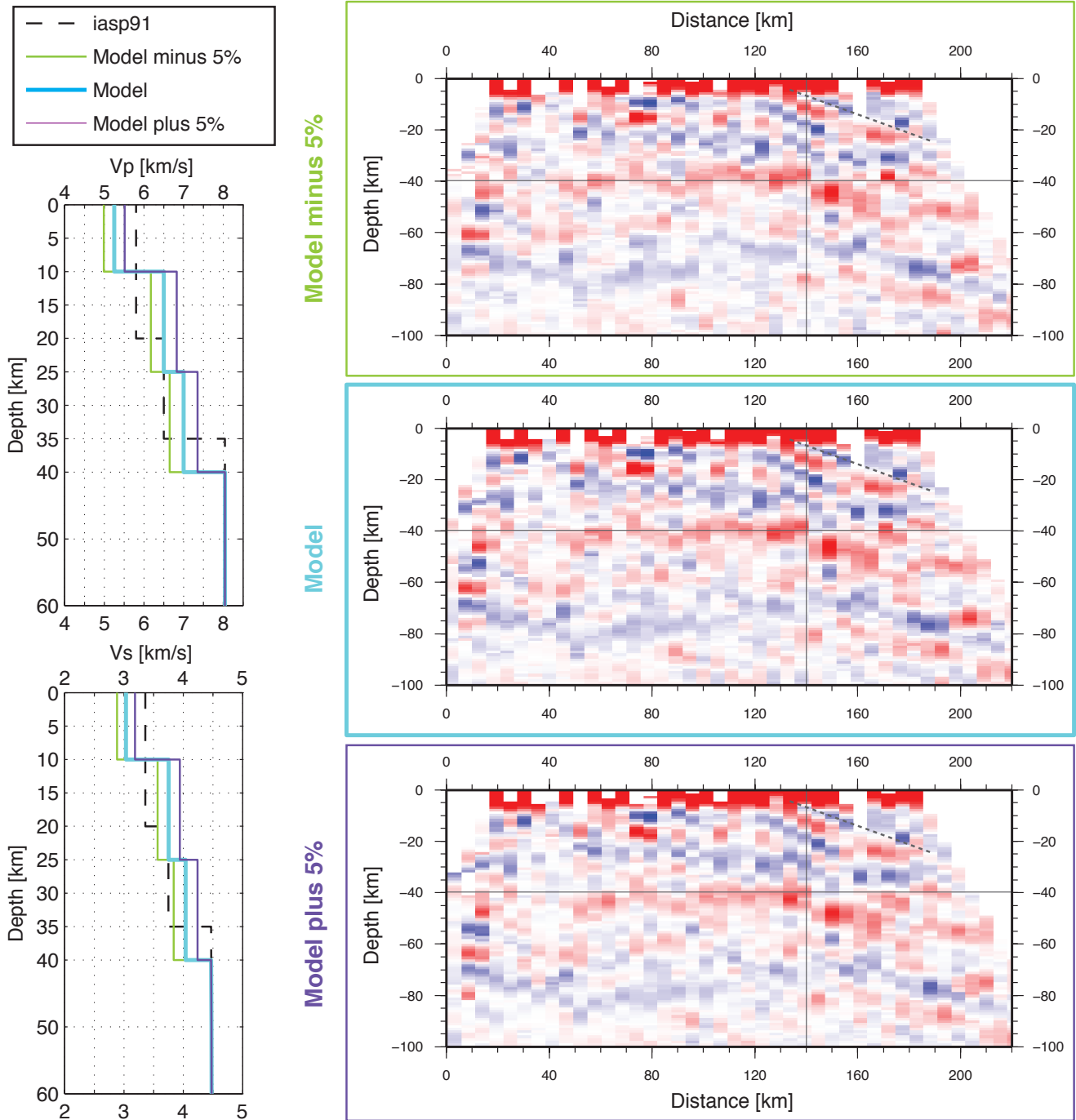


Figure S3: Common conversion point (CCP) receiver function stacks showing the effects of back projection with different velocity models. These are raw stacks (unmasked, unsmoothed, uninterpolated).  $V_p/V_s = 1.73$  for all three panels. ‘Model’ indicates the velocity model described in the main text, compiled from the literature, and used for all other CCP stacks in this paper (this panel is identical to the central panel of Figure S4). Fiducial lines at depth 40 km, lateral position 140 km, and along the interpreted MCT (dashed), are in the same location in each panel (and also in Figure S4) to allow easy assessment of the minor changes between each image.

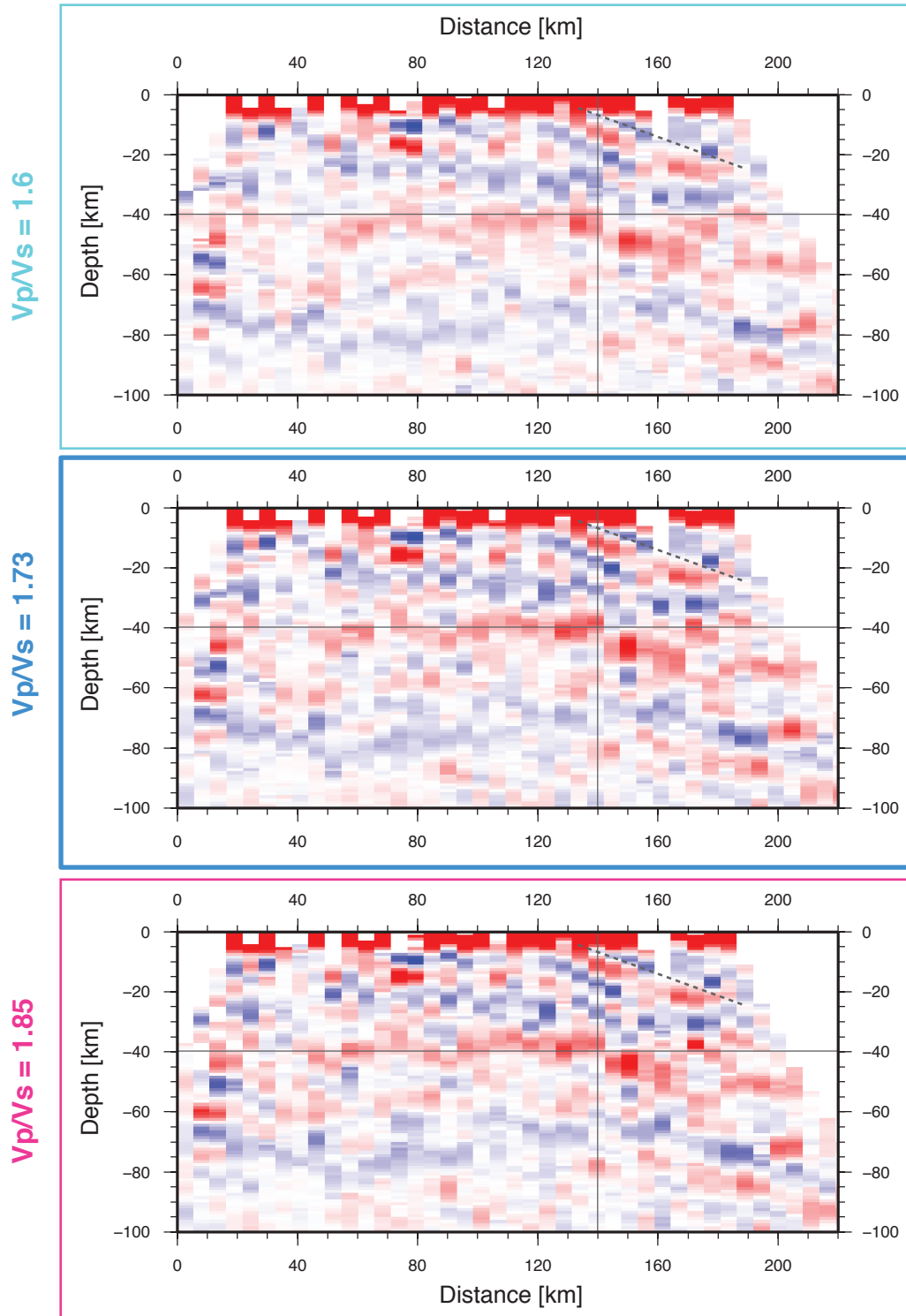


Figure S4: Common conversion point (CCP) receiver function stacks showing the effects of back projection with velocity models of different  $V_p/V_s$  ratio. These stacks are raw stacks (unmasked, unsmoothed, uninterpolated). Central panel with  $V_p/V_s = 1.73$  is identical to the central panel of Figure S3.  $V_p/V_s = 1.73$  used for all other CCP stacks in this paper. Fiducial lines as in Figure S3.

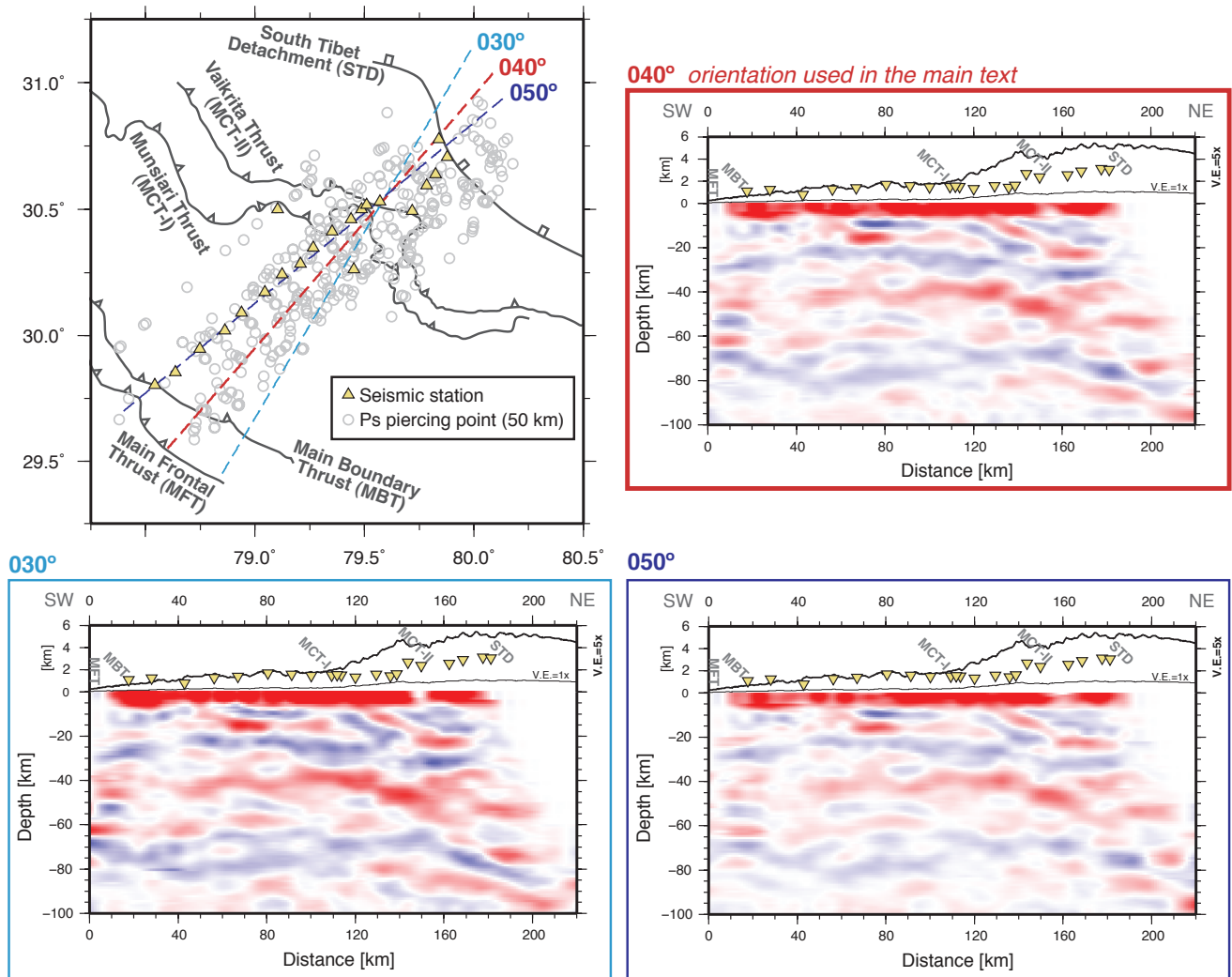


Figure S5: Common conversion point (CCP) receiver function stacks showing the effects of varying the orientation of the line of projection for CCP stacking. These stacks are smoothed and interpolated versions of the non-bootstrapped/non-masked stack. Top left panel shows locations of stations, major faults, piercing points of teleseismic rays at 50 km depth, and three different profile orientations (030°, 040°, 050°). Orientation 040° is used in the main text, and all other figures.